Two-Phase Compositional Flow Simulation in Complex Fractured Media by 3D Unstructured Gridding with Horizontal and Deviated Wells

Ali Zidane and **Abbas Firoozabadi,** Reservoir Engineering Research Institute

Summary

A higher-order numerical model for compositional two-phase flow in fractured media is presented in this paper. The simulation of horizontal and deviated wells is incorporated in the formation using unstructured grids. All commonly used types of finite elements are accounted for in the algorithm: quadrangular and triangular elements in 2D, and hexahedra, prisms and tetrahedra elements in 3D.

The fracture crossflow equilibrium (FCFE) approach is applied to model the flow exchange between the fractures and the matrix. FCFE is combined with the hybridized form of the mass conservative mixed finite element (MHFE) and the higher-order discontinuous Galerkin (DG) method. A computer-aided design (CAD) interface is developed that connects the mesh generator to the CAD software. The interface allows to design, mesh, and incorporate horizontal and deviated wells into the higher-order simulator. The algorithm allows flow simulation in fractures in all ranges of permeability values as opposed to the embedded discrete fracture matrix (EDFM) approach where low permeable fractures affect the accuracy of the results. The efficiency, accuracy, and strengths of the model are demonstrated in comparison to alternatives including the embedded discrete fracture approach in different examples. Detailed incorporation of complex wells is presented in this work.

Introduction

A substantial amount of the hydrocarbon reserves is in the naturally fractured reservoirs. Efficient exploitation of these reservoirs is facilitated using compositional reservoir simulators that have accuracy and computational efficiency.

Modeling of fractured reservoirs is challenging because fractures impose a large range of spatial properties. In addition, fractures may make the geometry more complex. Different approximations have been made in the literature to model fractured reservoirs (Bastian et al. 2000; Bogdanov et al. 2003; Geiger et al. 2004; Martin et al. 2005; Hoteit and Firoozabadi 2008; Reiter et al. 2012; Zidane and Firoozabadi 2014, 2015, 2017; Makedonska et al. 2015; Abushaikhaa et al. 2015; Ahmed et al. 2015a; Bahrainian and Daneh 2014; Chen et al. 2015; Hyman et al. 2015; Nejati et al. 2015). Structured grids may not describe various geometrical complexities. Unstructured gridding is the method of choice to describe complex fractured porous media (Heinemann et al. 1991; Naccache 1997; Karypis and Kumar 1998; Beckner et al. 2001, 2006; Usadi et al. 2007; Liu et al. 2009).

The numerical approaches in fractured reservoir simulation are broadly divided into two categories: continuous representations as in dual-porosity (DP)/dual-permeability (DK) models (Barenblatt et al. 1960; Warren and Root 1963; Kazemi and Gilman 1969, 1992; Kazemi et al. 1976; Kazemi and Merrill 1979; Gilman and Kazemi 1983; Quandalle and Sabathier 1989; Sarda et al. 2002; Lu et al. 2008; Fung and Du 2016; Ozkaya 2017) and discrete representations in the form of discrete fracture/discrete matrix model (DFDM or DFM) (Thomas et al. 1983; Haggerty and Gorelick 1995; Kim and Deo 2000; Di Donato et al. 2004; Karimi-Fard et al. 2004; Martin et al. 2005; Reichenberger et al. 2006; Matthai et al. 2007a, 2007b; Gouze et al. 2008; Hoteit and Firoozabadi 2008; Geiger et al. 2009; Unsal et al. 2010; Nick and Matthai 2011; Sandve et al. 2012; Geiger et al. 2013; Schmid et al. 2013; Jiang and Younis 2016).

One variant of the DFM approach is the EDFM. The EDFM approach was first proposed by Lee et al. (2001) and later adopted by Li and Lee (2008), Hajibeygi et al. (2011), Moinfar et al. (2014), and Yan et al. (2016). In this work, we refer to EDFM and DFM as separate entities. In the DFM models, the matrix domain is discretized to describe the fracture positions. The matrix grid cells conform to the fracture elements. The matrix–fracture exchange fluxes are modeled explicitly (Hui et al. 2018).

In the EDFM models, the fracture elements are embedded in the matrix grid cells, and virtual grids are created to represent the fractures (Yu et al. 2017). Four types of connections are considered in the EDFM models: flow between matrix grid cells and the fracture elements, flow between fracture elements within one fracture, flow between intersecting fracture elements, and flow between fractures and the well (Yu et al. 2017). In EDFM, a structured Cartesian grid may be used even if the fractures have different orientations. This will allow the EDFM model to be implemented in finite difference (FD) simulators. EDFM enables the modeling of irregular fracture geometry in Cartesian grids, but in case of high-saturation contrast, an adaptive grid refinement is required which affects the efficiency (Jiang and Younis 2016; Hui et al. 2018). To overcome the limitations of the DP models, a hybrid model that combines DP and EDFM has been proposed (Amir and Sun 2017; Weirong et al. 2017).

Unstructured grids have gained popularity in flow modeling and simulation (Aavatsmark et al. 1998, 2010; Edwards and Zheng 2010; Lamine and Edwards 2010; Moortgat and Firoozabadi 2016) with many advantages over the Cartesian grids. These include the ease to simulate fractured reservoirs in which fractures have different orientations and incorporation of deviated wells (DWs) in the domain.

In this work, we use the DFM concept as in the past. Our algorithm includes the commonly used finite elements (FEs) in 2D and 3D, namely, quadrangular and triangular elements in 2D and hexahedral, prismatic, and tetrahedral elements (structured and unstructured) in 3D. The fracture aperture is assumed to be small compared to the matrix scale (Noorishad and Mehran 1982; Granet et al. 1998; Martin et al. 2005; Hoteit and Firoozabadi 2005). The fractures are, therefore, represented by a lower dimension compared to the dimension in the matrix domain. We apply the FCFE approach in our DFM mode (Zidane and Firoozbadi 2017). In FCFE, we assume a

This paper (SPE 191405) was accepted for presentation at the SPE Annual Technical Conference and Exhibition, Dallas, Texas, USA, 24–26 September 2018, and revised for publication. Original manuscript received for review 1 March 2019. Revised manuscript received for review 9 September 2019. Paper peer approved 12 September 2019.

constant pressure across the fracture width. This alleviates the need for small elements in the matrix domain near the fractures. The fractures are represented by the edges of the FEs in FCFE. This makes FCFE readily applicable to unstructured grids in 2D and 3D.

In addition to fractures, multiphase flow in vertical and horizontal wells is of general interest in subsurface formation flows. In many cases, the wellbore is deviated and, in some cases, highly inclined (Stanlsav et al. 1990). DWs increase the reservoir reach and improve deliverability (Ghahri et al. 2011). Wellbore deviation adds more complexity to multiphase flow modeling (Hasan and Kabir 1988). Various studies have been conducted to study the pressure drop and flow patterns in inclined tubes and DWs (Beggs and Brill 1973; Barnea et al. 1985; Hasan and Kabir 1988; Stanlsav et al. 1990). There is an extensive use of DWs with high deviation ramps in some formations. The hole deviation could exceed 70°, and the ramp lengths may reach more than 3000 m (Escaron 1983; Kruger 2007). There is a need for reservoir simulation of complex wells and accurate production forecast.

Well modeling is traditionally accomplished through an idealization by Dirac line sources (Aziz and Settari 1979). The flow rate in well elements is calculated through the transmissibility terms on the basis of effective mobility. The pressure gradient used in modeling of flow around the well is the pressure difference between the bottomhole pressure and the average pressure in the gridblock. Collins et al. (1992) presented a model to simulate wellbore dynamics. Nghiem et al. (1992) discussed the important factors that influence the simulation of DWs and horizontal wells. They used a line sink model. In a DP simulator, Sanchez et al. (1992) showed that in naturally fractured reservoirs, the high-inclined wells improve oil production performance. Sanchez et al. (1992) simulated a well with a 55° inclination angle to show increased production performance compared to a vertical well. In a recent study (Artus et al. 2017), the well is modeled by 3D unstructured grids in a reservoir discretized with 2.5D Voronoi grids. In order to capture the well trajectory (Artus et al. 2017), the gridblocks intercepting the well trajectory are removed from the 2.5D grids and filled with finer 3D grids constrained to well geometry. We follow a similar technique, but 3D grids are used in the whole domain to alleviate using finer grids in the wellbore.

In our previous work, we have applied the FCFE approach in single-phase flow (Zidane and Firoozabadi 2014) and then extended the approach to compositional two-phase flow in 2D structured grids (Zidane and Firoozbadi 2017). In this work, we apply our FCFE approach to compositional two-phase flow in fully 3D unstructured grids. In addition, we present the first implementation of horizontal and deviated fractured wells in our higher-order numerical model. We discretize the wellbore with unstructured grids in 3D, and readily match the well geometry with the reservoir matrix domain. To overcome the computational cost of the small well elements, we remove the well gridblocks from the domain and redistribute the well flow rate across the interfaces of the well elements. In this work, we neglect the flow mechanics inside the wellbore, and we only consider the effect on the reservoir flow behavior. The wellbore hydraulics affect the inflow profile near wellbore region and can be studied separately. The use of fully unstructured grids in 3D in our model avoids the limitation imposed by pillar-type FEs as prismatic or Voronoi grids. A full description of well implementation in our model will be discussed in Appendix A.

The rest of this paper is organized as follows: We provide a general description of the model and the differential equations describing the flow in fractured porous media in the FCFE concept. Then, we present a brief overview of the numerical discretization in the matrix and the fracture network. This is followed by five numerical examples to demonstrate the strengths of our proposed algorithm and the ease with which one can incorporate complex wells in a higher-order simulator.

Model Description

We briefly outline the essence of the algorithm as follows:

- The fluxes in the matrix domain and the fracture network are calculated by the RT0 hybridized MHFE (Younes et al. 2013, 2015; Huggenberger et al. 2015; Moortgat and Firoozabadi 2016). The MHFE method is used to avoid the complexity and numerical oscillations that could be produced from the two-point flux approximation (TPFA) and the multipoint flux approximation (MPFA). Later, MPFA implementations do not suffer from the induced oscillations (Aavatsmark et al. 2010; Edwards and Zheng 2010; Lamine and Edwards 2010; Sandve et al. 2012). In MHFE, the traces of pressure at the element interfaces and the pressure at the cell centers are calculated. The MHFE is a natural choice for implementation in unstructured gridding (Darlow et al. 1984; Mosé et al. 1994; Hoteit and Firoozabdi 2008; Ackerer and Younes 2008; Younes et al. 2011, 2014, 2015; Zidane et al. 2012, 2014a, 2014b; Zidane and Firoozabadi 2018a, 2018b). The effect of capillary pressure is not included in this work. This is justified by the low interfacial tension (IFT) in compositional two-phase (oil and gas) flow at high pressure.
- The mass balance equations in the matrix domain are discretized using the mass conservative DG method coupled with a slope limiter to remove the nonphysical oscillations (Chavent and Jaffré 1986; Hoteit et al. 2004). The degrees of freedom in DG are the number of nodes at the element level. In addition, DG is a convenient method to capture the discontinuities in phase composition at the element interfaces. In the fracture network, the finite volume (FV) method is used.
- The traces of the pressure are implicitly calculated at the interfaces in both matrix and fractures. An implicit time scheme is also used to solve for the molar densities of all components in the fracture network. In the matrix domain, an explicit time scheme is used to update the molar densities.
- Quadrangular and triangular elements are used in 2D and hexahedral, prismatic, and tetrahedral elements in 3D.
- The algorithm includes an interface to CAD software and to tetgen (Si 2011) to design and generate complicated domain geometries, fractures, and DWs. The details of well implementation are presented in Appendix A.
- Local thermodynamic equilibrium and phase stability are implemented (Li and Firoozabadi 2012). The phase and volumetric behavior are described by the Peng–Robinson equation of state (EOS) (Peng and Robinson 1976).

Mathematical Model

For completeness, the main equations that govern the compositional multiphase flow in fractured media are presented in this section. The governing equations in the matrix domain and the fractures are treated separately.

Matrix Domain. In compressible two-phase flow, the mass transport equations for component i in an n_c-component mixture are given by

$$\phi\frac{\partial cz_i}{\partial t}+\nabla\cdot\left(\sum_{\alpha}c_\alpha x_{i,\alpha}\boldsymbol{v}_\alpha\right)=F_i,\quad i=1,\ldots,n_c\quad\text{in}\quad\Omega\times(0,\tau), \qquad (1)$$

and

$$\sum_{i=1}^{n_c}z_i=\sum_{i=1}^{n_c}x_{i,\alpha}=1, \qquad (2)$$

where ϕ denotes the porosity; $\boldsymbol{v}_\alpha$ is the velocity of Phase α; c is the overall molar density of the mixture; z_i and F_i are the overall mole fraction and the sink/source term of Component i in the mixture, respectively; c_α is the molar density of Phase α; $x_{i,\alpha}$ is the mole fraction of Component i in Phase α; Ω is the computational domain; τ denotes the simulation time; and n_c is the number of components. We neglect diffusion in Eq. 1.

The velocity of Phase α is given by Darcy's law:

$$\boldsymbol{v}_\alpha = -\frac{\mathbf{K}k_{r\alpha}}{\mu_\alpha}(\nabla p - \rho_\alpha \mathbf{g}) = -\lambda_\alpha \mathbf{K}(\nabla p - \rho_\alpha \mathbf{g}), \quad \alpha = o, g, \quad \ldots\ldots\ldots\ldots (3)$$

where $\mathbf{K}$ is the absolute permeability; $k_{r\alpha}$, μ_α, and ρ_α are the relative permeability, dynamic viscosity, and mass density of Phase α, respectively, with $\lambda_\alpha = k_{r\alpha}/\mu_\alpha$; p is the pressure; and $\mathbf{g}$ is the gravitational acceleration. We use the method from Lohrenz et al. (1964) to describe the phase viscosities.

The pressure equation on the basis of the total volume balance is given by (Acs et al. 1985; Watts 1986)

$$\phi C_t \frac{\partial p}{\partial t} + \sum_{i=1}^{n_c} \overline{V}_i \nabla \cdot \left(\sum_\alpha c_\alpha x_{i,\alpha} \boldsymbol{v}_\alpha \right) = \sum_{i=1}^{n_c} \overline{V}_i F_i, \quad \ldots\ldots\ldots\ldots (4)$$

where C_t is the total compressibility and $\overline{V}_i$ is the total partial molar volume of Component i (Firoozabadi 2015).

The phase equilibrium calculation is on the basis of initial guess from stability analysis. The minimum Gibbs free energy is warranted. From the local thermodynamic equilibrium, the equality of the fugacities of each component in the two phases (oil and gas) is given as follows:

$$f_{o,i}(T, p, x_{j,o}) = f_{g,i}(T, p, x_{j,g}), \quad i = 1, \ldots, n_c; \quad j = 1, \ldots, n_c - 1. \quad \ldots\ldots\ldots\ldots (5)$$

Fracture Network. In the fracture elements, the mass balance equations are given by

$$\phi \frac{\partial c z_i}{\partial t} + \nabla \cdot \left[\sum_\alpha c_\alpha x_{i,\alpha} \left(\boldsymbol{v}_\alpha - \boldsymbol{v}_\alpha^{fr} \right) \right] = F_i, \quad \ldots\ldots\ldots\ldots (6)$$

$\boldsymbol{v}_\alpha$ is the velocity across the fracture width and $\boldsymbol{v}_\alpha^{fr}$ is the velocity in the direction of fracture length.

The pressure equation in the fractures is given by

$$\phi C_t \frac{\partial p}{\partial t} + \sum_{i=1}^{n_c} \overline{V}_i \left\{ \nabla \cdot \left[\sum_\alpha c_\alpha x_{i,\alpha} \left(\boldsymbol{v}_\alpha - \boldsymbol{v}_\alpha^{fr} \right) \right] - F_i \right\} = 0. \quad \ldots\ldots\ldots\ldots (7)$$

The above equations are integrated along the fracture width.

Discretization

We briefly describe the discretization of the flow and transport equations in the following. The total velocity is discretized in the MHFE method. The flux at each interface is evaluated as a function of the traces of the pressure at the interface and the pressure at the center of each FE as follows:

$$q_{K,E} = \alpha_{K,E} p_K - \sum_{E' \in \partial K} \beta_{K,E,E'} t p_{K,E'} - \gamma_{K,E}. \quad \ldots\ldots\ldots\ldots (8)$$

The coefficients $\alpha_{K,E}$, $\beta_{K,E,E'}$, and $\gamma_{K,E}$ depend on the geometry of the element; the details of the MHFE formulation can be found in previous studies (Chavent et al. 1990; Brezzi and Fortin 1991; Chavent and Roberts 1991; Mosé et al. 1994).

The FV integration of the pressure equation in the matrix domain gives

$$\phi |K| C_t \frac{\Delta p}{\Delta t} + \sum_{i=1}^{n_c} \overline{V}_{i,K} \left[\sum_\alpha \sum_{E \in \partial K} \int_E c_\alpha x_{i,\alpha} f_\alpha (\boldsymbol{v} + \boldsymbol{G}_\alpha) \cdot \boldsymbol{n}_E - F_{i,K} \right] = 0. \quad \ldots\ldots\ldots\ldots (9)$$

And in the fracture network, we obtain

$$\phi C_t |k| \frac{\Delta p}{\Delta t} + \sum_{i=1}^{n_c} \overline{V}_{i,k} \begin{bmatrix} \sum_e \int_e \sum_\alpha c_\alpha x_{i,\alpha} f_\alpha (\boldsymbol{v} + \boldsymbol{G}_\alpha) \cdot \boldsymbol{n}_e \\ - \sum_{Ei} \int_{Ei} \sum_\alpha c_\alpha x_{i,\alpha} \boldsymbol{v}_\alpha^{fr} \cdot \boldsymbol{n}_{Ei} - |k| F_i \end{bmatrix} = 0. \quad \ldots\ldots\ldots\ldots (10)$$

To discretize the mass balance equations, the DG method is used in the matrix domain and the FV method in the fracture network. In DG, the mass balance equations are multiplied by a shape function and integrated over each matrix element K; this gives

$$\int_K \phi \frac{\partial c z_i}{\partial t} \varphi_{K,j} + \sum_E \int_E \sum_\alpha (\overline{c_\alpha x_{i,\alpha}} \boldsymbol{v}_\alpha) n_E \varphi_{K,j} - \int_K \sum_\alpha (c_\alpha x_{i,\alpha} \boldsymbol{v}_\alpha) \nabla \varphi_{K,j} = \int_K F_i \varphi_{K,j}. \quad \ldots\ldots\ldots\ldots (11)$$

The FV integration over the mass balance equations in the fractures gives

$$\phi |k| \frac{c z_{i,k}^{n+1} - c z_{i,k}^n}{\Delta t} + \sum_\alpha \left[\sum_{e \in \partial k} \left(\overline{c_\alpha x_{i,\alpha}}^{n+1} q_{\alpha,k,e} \right) - \overline{Q}_{\alpha,i}^{fr} \right] = |k| F_i. \quad \ldots\ldots\ldots\ldots (12)$$

For the temporal discretization, an explicit time scheme is used in the matrix and an implicit time scheme in the fractures. $\overline{Q}^{fr}_{\alpha,i}$ in the above equation denotes the exchange flux of Component i in Phase α between the fracture and the adjacent matrix elements.

When multiple fractures intersect **(Fig. 1),** the upstream value at the interface is evaluated using a combination of the conservation of mass and Kirchhoff's law (Ahmed et al. 2015b; Zidane and Firoozabadi 2017).

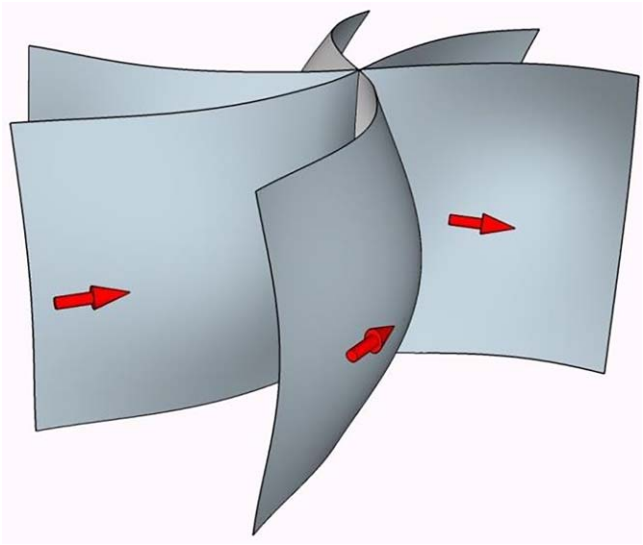

Fig. 1—Fracture intersection in 3D; red arrows show flow directions.

Numerical Examples

We present five numerical examples. In these examples, the components in the petroleum fluids vary from 2 to 8 in 2D and 3D domains. An Intel® Core™-i5 PC, with 3-GHz central processing unit (CPU) and 4-GB RAM, is used in all runs.

Example 1: Quarter of Five Spot and Comparison with Finite Element–Finite Volume. In this example, the effect of mesh refinement is examined in triangular elements in a quarter of a five spot with the fractures presented by Geiger et al. (2009). The domain contains 12 interconnected fractures as shown in **Fig. 2.** The matrix domain has a permeability of 100 md and 20% porosity. The fracture permeability is 1000 darcies. CO_2 is injected into the formation saturated with an equimolar mixture of ethane and propane. Injection and production wells are located at the origin and the diagonally opposite corner, respectively. Similar to Geiger et al. (2009), six different levels of mesh refinements are used. We show in Fig. 2 the different meshes with the number of elements in each mesh. The effect of mesh refinement is evaluated by computing the L^2 norm of error of gas saturation assuming the fine grid solution to be exact. We compare the L^2 norm of error in our model with the finite element–finite volume (FEFV) model presented in Geiger et al. (2009). The type of flow (compositional two-phase) in our model is different from the black oil model used in Geiger et al. (2009). However, comparing the L^2 norm of gas saturation in both models may give a picture on the overall performance in terms of number of elements. For simplicity, we evaluate the L^2 norm of error as a function of the relative FE area (i.e., area of FE divided by total area of the domain). As shown in **Fig. 3,** the L^2 norm of error of the gas saturation in our model is less than that in FEFV model for all levels of refinement. Material balance error (in terms of number of moles) is within a range of 10^{-13} in this example and will be discussed in more detail later.

In addition to the L^2 norm of error, the CPU time with different meshes in the FCFE and FEFV models is presented in **Table 1.** The large difference in the CPU time shown in Table 1 is partly related to the computational resources available at the time. However, indications are that our algorithm is faster than the FEFV model. The details of the simulation platform used are provided earlier. For reference, the gas saturation and the overall mole fraction of CO_2 at different pore volume injections (PVIs) are shown in **Fig. 4.** Note that assigning different permeability values across the normal and the lateral sides of the fractures is readily achieved in our algorithm as discussed in Appendix B.

Example 2: Comparison with EDFM. A comparison of the proposed algorithm with EDFM approach is presented in this example. The example is originally reported in Moinfar et al. (2014). A mixture of CO_2 and CH_4 is injected in a fractured domain saturated with a three-component oil. The compositions of the injected and reservoir fluids are presented in **Table 2.** The domain is shown in **Fig. 5.** The injection well is located at one corner and production is at the opposite corner where the pressure is kept constant. The relevant data are summarized in **Table 3.** The CPU time in the proposed algorithm for a simulation time of 600 days is 5.1 minutes in an Intel Core-i5 PC, with 3-GHz CPU and 4-GB RAM. In Moinfar et al. (2014), enough information was not provided on the platform used in the simulations; therefore, direct comparison of CPU time might not reflect a fair comparison of performance. Moinfar et al. (2014) report CPU time of 24.6 minutes. In Moinfar et al. (2014), a standard FD modeling was used in a domain that consists of $30 \times 15 \times 1$ matrix grids and 40 fracture grids. In the proposed algorithm, a higher-order discretization model is used. Furthermore, in compositional modeling, flash calculation is performed at all nodes of each FE in addition to flash calculation at the center of the element. In a hexahedral FE, there are nine flash calculations per FE. Added to the cost of DG and MHFE compared with FD, this demonstrates the efficiency of the proposed algorithm. For reference, the gas saturation at 35% PVI is shown in **Fig. 6.** Note that the same number of gridding is used as in Moinfar et al. (2014).

Example 3: Comparison with the EDFM/DPDP Hybrid Model. In this example, a fractured domain is considered that has the same properties of matrix and fractures as in Weirong et al. (2017) with the difference of CO_2 injection in propane instead of water injection in oil. The relevant data are presented in **Table 4.** The model in Weirong et al. (2017) is a hybrid combination of EDFM and DPDP.

It is known that the EDFM produces inaccurate results when the fractures permeability is low (Tene et al. 2017; Weirong et al. 2017). In the proposed algorithm, all range of fracture permeabilities can be simulated. A set of randomly distributed fractures with different lengths are generated. Impermeable fractures are added to demonstrate this feature in our model. The domain and the fracture network including the impermeable faults are shown in **Fig. 7** (fractures shown in blue and impermeable faults in red). Geometric information for all fractures and impermeable faults is provided in Appendix C. CO_2 is injected in the middle of the domain. Production is from the four corners. Location of the injection and production wells is shown in Fig. 7a; the injection and production wells cross the domain in all the vertical depths. Simulations were run with different mesh refinements as shown in **Table 5,** and using a mesh of 41,000 elements as a reference solution; further refinement did not affect the results. The different meshes are shown in **Fig. 8.**

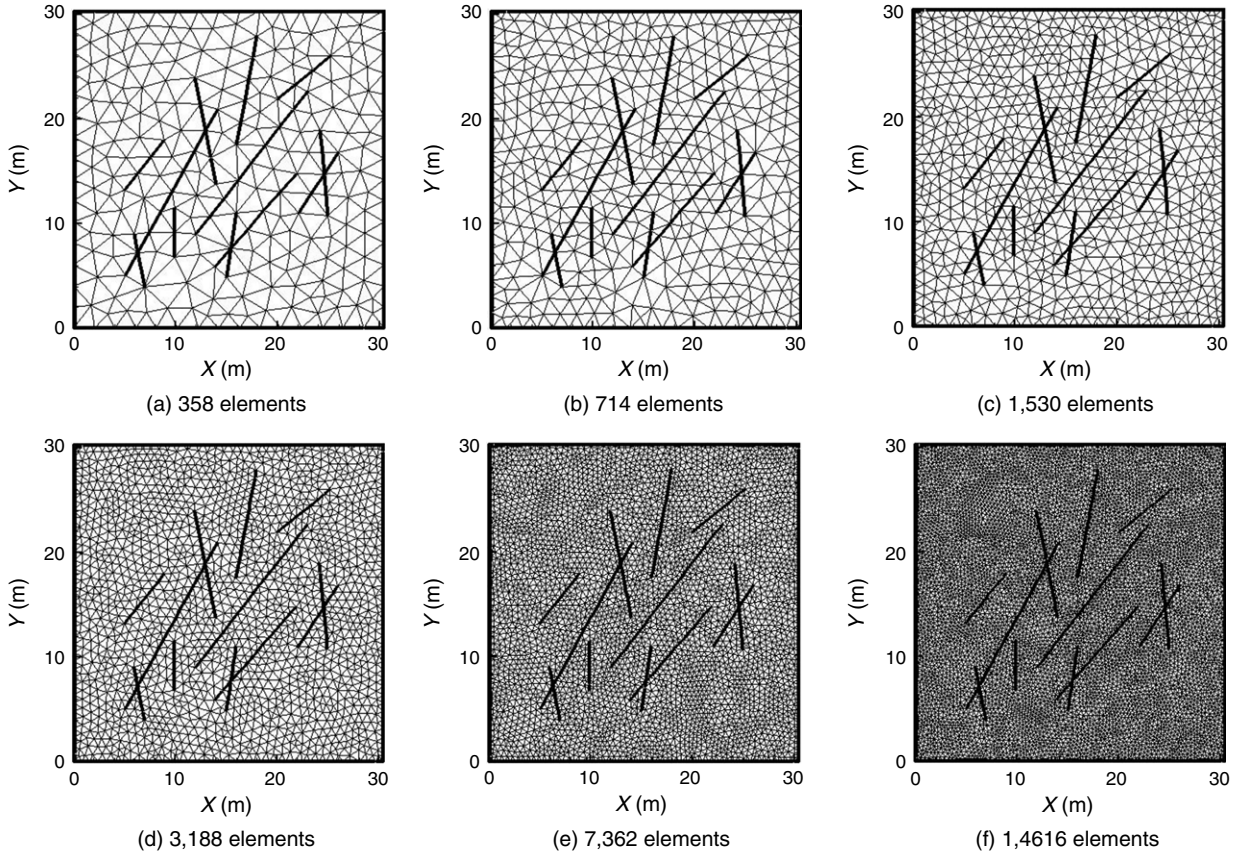

Fig. 2—Different mesh refinements: Example 1.

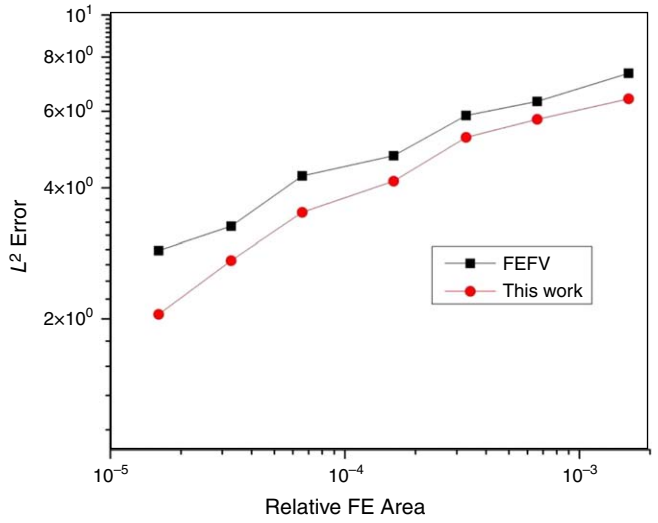

Fig. 3—Relative L^2 norm error of the gas saturation: Example 1.

FEFV (Geiger et al. 2009)		This Work	
Number of Elements	CPU (seconds)	Number of Elements	CPU (seconds)
342	2,076	358	162
734	3,662	714	294
1,502	8,818	1,530	410
3,190	23,989	3,188	741
7,348	98,184	7,362	2,489
14,326	278,501	14,616	5,779
29,132	776,313	30,730	10,805

Table 1—CPU time for different mesh refinements: Example 1.

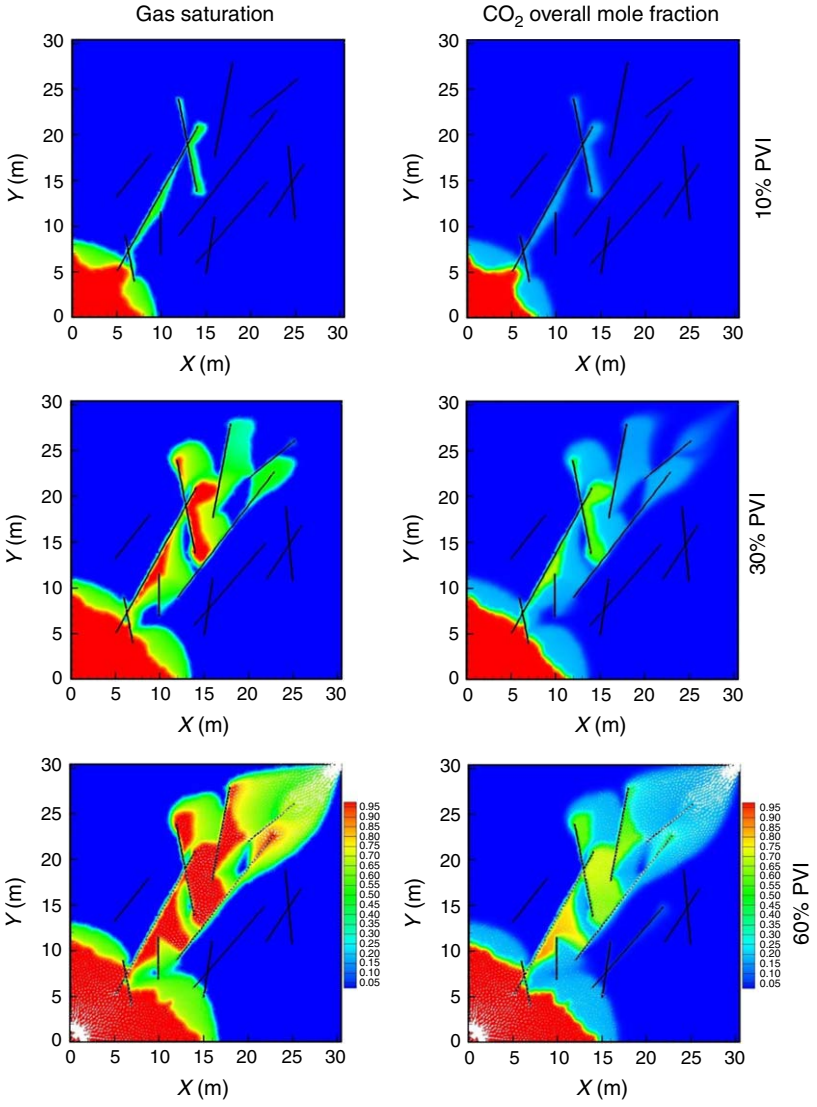

Fig. 4—Gas saturation at different PVIs, and the velocity of gas phase at 60% PVI (white vectors): Example 1.

Component	Injected Fluid (%)	Reservoir Fluid (%)
CO_2	98	1
CH_4	2	39
$C_{16}H_{34}$	0	60

Table 2—Composition of injected and reservoir fluids (in mole %): Example 2.

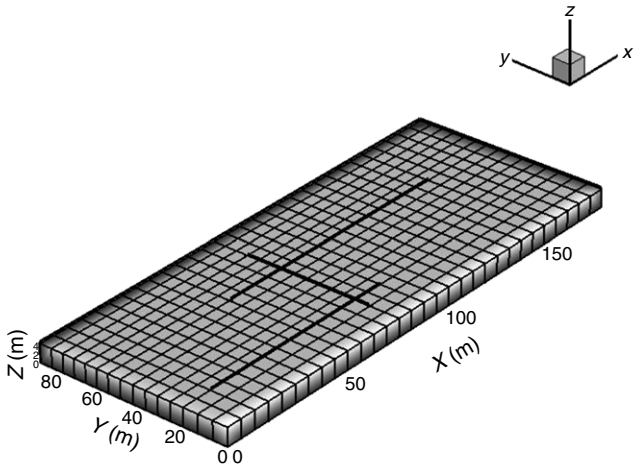

Fig. 5—Domain with fractures: Example 2.

Parameter	Value
Pressure (bar)	69
Temperature (K)	344
Porosity (%)	10
Matrix permeability (md)	1
Fracture permeability (md)	$8–10^4$

Table 3—Relevant data: Example 2.

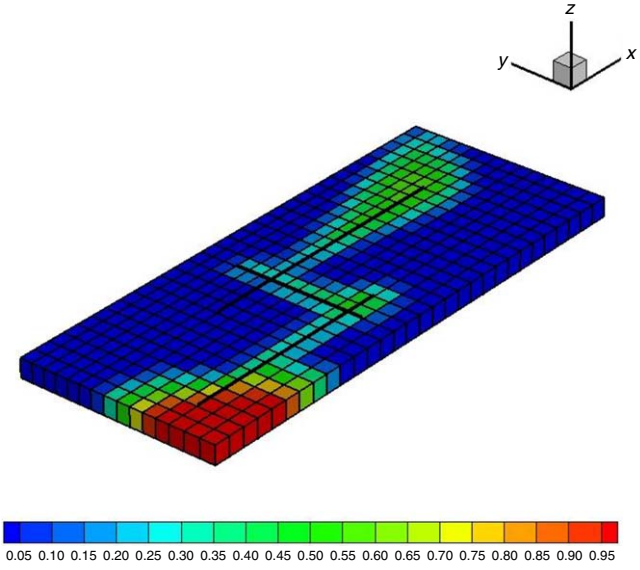

Fig. 6—Gas saturation at 35% PVI: Example 2.

Parameter	Value
Matrix permeability (md)	1
Fracture permeability (darcies)	500
Fracture width (ft)	0.0065
Porosity (%)	5
Pressure at the bottom (bar)	25
Temperature (K)	311
Domain size (ft^3)	$1{,}000 \times 1{,}000 \times 20$

Table 4—Relevant data: Example 3.

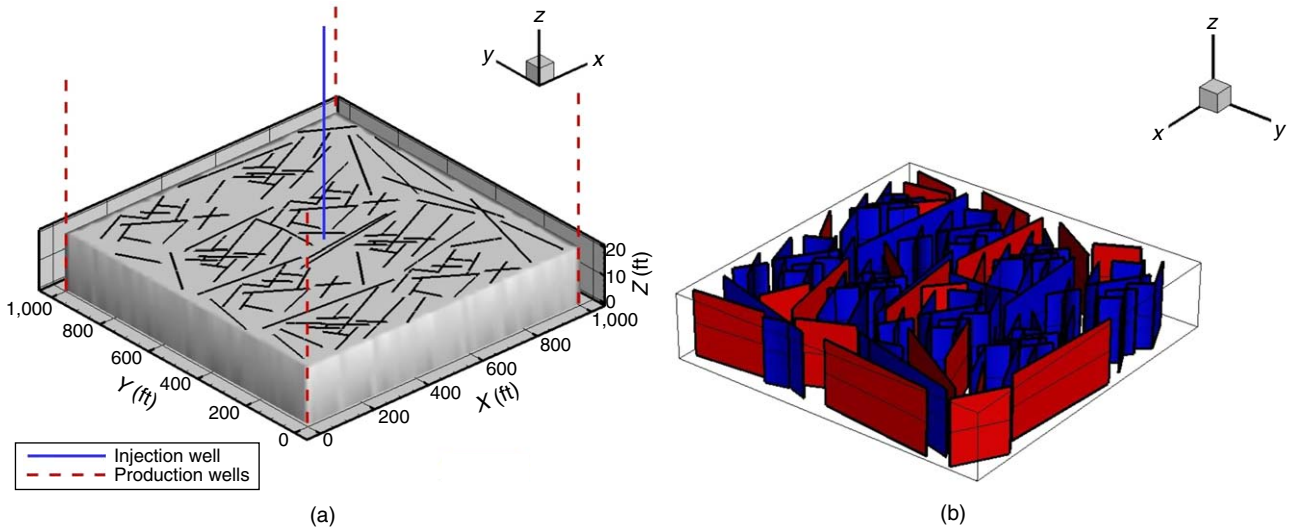

Fig. 7—(a) Domain and (b) fractures in blue and faults in red: Example 3.

Mesh	Number of Nodes	Number of Elements	Number of Interfaces	CPU Time (seconds)
Mesh a	804	1,044	3,144	127
Mesh b	1,524	1,876	5,704	285
Mesh c	4,833	6,128	18,540	1,714
Mesh d	7,668	9,828	29,680	2,570
Mesh e	31,944	41,796	125,784	10,285

Table 5—Number of nodes, elements, and interfaces in all meshes: Example 3.

The number of nodes, elements, and interfaces for all meshes is listed in Table 5. The oil recovery in different meshes is shown in **Fig. 9.** A good agreement is observed even when a very coarse mesh is used. Note that the fracture network in this example and in Weirong et al. (2017) is not the same; however, the fracture/matrix permeability ratio is the same. As reported in Weirong et al. (2017), the CPU time is 4,322 seconds in DFM, 268 seconds in EDFM, and 55 seconds in EDFM-DPDP. In the proposed algorithm, the simulation time is 127 seconds in Mesh a and 10,285 seconds in Mesh e. Weirong et al. (2017) report that the accuracy of EDFM-DPDP is slightly below the traditional EDFM method. For reference, the oil saturation at 45% PVI is shown in **Fig. 10** for both the matrix domain and the fracture network.

Example 4: Horizontal Well. This example is inspired from Tang et al. (2018) with some changes. The domain size is $1200 \times 800 \times 100\,\text{m}^3$ and contains one horizontal well crossing the middle of the formation for CO_2 injection. The injection well of 5½ in. diameter has a total length of 800 m with 45° inclination. Four production wells are located at the four corners of the domain. The domain with the injection and production wells is shown in **Fig. 11.** CO_2 is injected at a constant rate of 0.1 PV/yr. The composition of the initial oil is shown in **Table 6.** The domain has 11 fractures with 8 crossing the horizontal well as shown in Fig. 11. Relevant data of the domain are shown in **Table 7.** Simulations were run with three different mesh refinements varying from 5,000 to 23,000 elements (Meshes 1–3). The refined mesh of 75,000 elements (Mesh 4) is a reference solution mesh. The reference mesh is used to calculate the relative L^2 norm of error of the gas saturation for the three different meshes. The total number of matrix and fracture elements is shown in **Table 8. Fig. 12** reveals that the error drops to less than 5% for the 23,000-element mesh, an acceptable variation for a complicated problem with fully compositional flow. The CPU time in the aforementioned mesh is 7 hours. Note that the CPU time could be reduced by coarsening the well geometry as we discuss in Appendix A. Coarsening the well increases the size of the matrix elements near the well region, thus reduces the CPU time but affects the geometry of the well.

Example 5: Deviated Well. This example is inspired from Artus et al. (2017). The geometry of the boundary is kept the same as that in Artus et al. (2017); the domain dimensions in this example are $1000 \times 1000 \times 200\,\text{m}^3$ **(Fig. 13a).** The domain includes a DW inclined at three different angles in 3D with the same well diameter used as in the previous example. Production is performed at constant pressure at the bottom left and right corners of the domain as shown in Fig. 13a. The domain geometry is shown in Fig. 13a, and the well geometry and initial mesh (see Appendix A for details) are shown in Figs. 13b and 13c, respectively. Fractured and unfractured domains are studied. The fractures have different shapes and dimensions, and some cross the wellbore. **Fig. 14** shows the domain with the fractures. The fractures have different shapes, dimensions, and orientations, and some cross the wellbore. The orientation of the fractures from vertical is as follows: for quadrangle fractures, the range assigned varies from 0° to 22.5° (randomly), and in circular shape fractures, the range of angles with vertical varies from 22.5° to 45° (randomly). The domain and fracture properties are the same as in Example 4. **Fig. 15** shows the oil recovery with and without fractures, and as expected, the recovery is affected by the fractures. The oil recovery in the fractured media is 10% less than in unfractured media (to 1.5 PVI). The CPU time for a total of 45,000 elements is 13 hours for fractured media and 10.6 hours for unfractured media. The difference in CPU time between fractured and unfractured media demonstrates that the simulation of a fractured media in the proposed algorithm is nearly within the same range of unfractured media. As mentioned earlier, CPU time could be reduced by coarsening the well geometry or adapting a different time discretization scheme. Depending on the simulation purpose, either one or both options could be implemented. Material balance error is within a range of 10^{-13} during the simulation time as shown in **Fig. 16.**

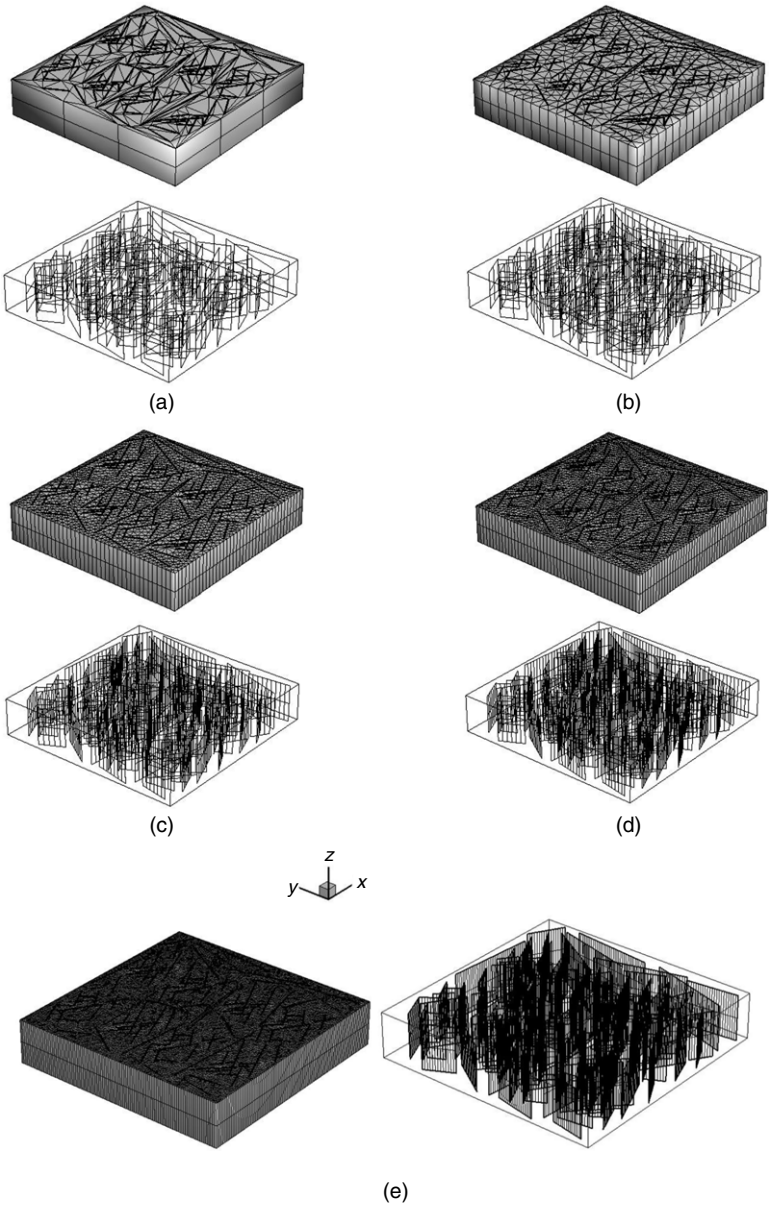

Fig. 8—Different mesh refinements in matrix and fractures (details of all meshes are shown in Table 5): Example 3.

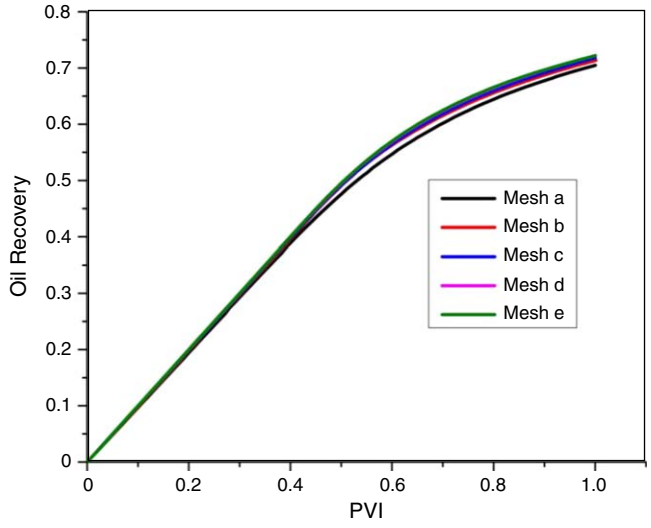

Fig. 9—Oil recovery with different meshes: Example 3.

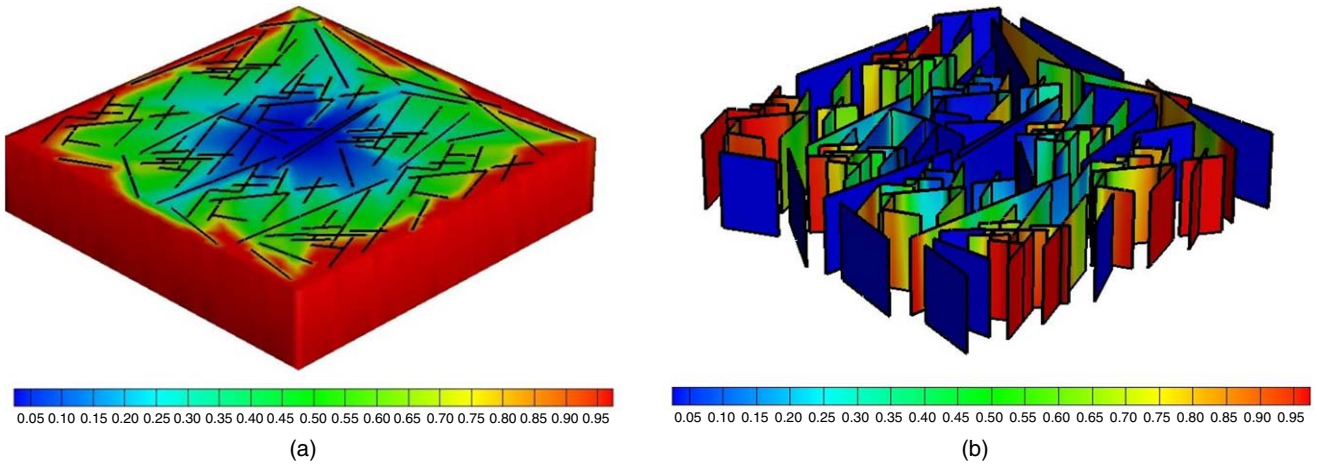

Fig. 10—Oil saturation at 45% PVI in (a) the matrix domain and (b) the fracture network: Example 3.

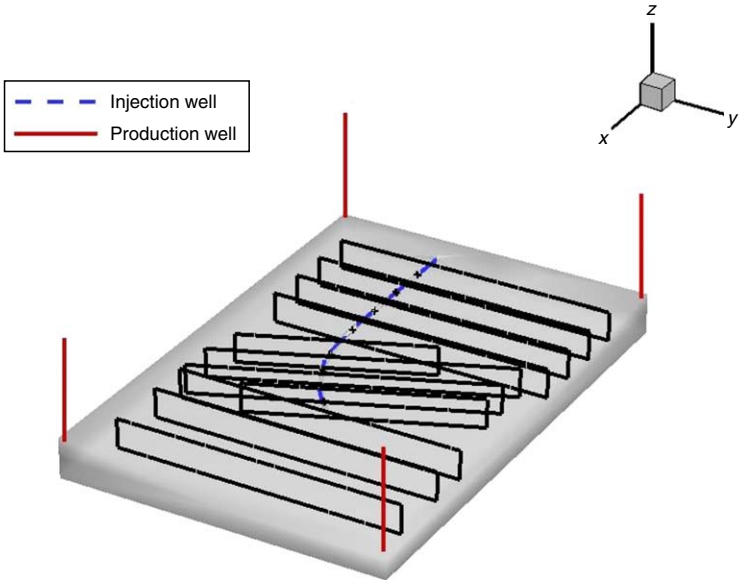

Fig. 11—Domain and location of injection and production wells. Horizontal well crossing the fractures is shown by dashed line: Example 4.

Component	Overall Mole Fraction
CO_2	0.0086
N_2	0.0028
C_1	0.4351
C_2–C_3	0.1207
C_4–C_5	0.0505
C_6–C_{10}	0.1328
C_{11}–C_{24}	0.166
C_{25+}	0.0735

Table 6—Oil composition: Example 4.

Property	Value
Matrix permeability (md)	100
Porosity (%)	20
Temperature (K)	403.15
Pressure at the bottom (bar)	276
Fracture width (mm)	1
Fracture permeability (md)	10^6

Table 7—Domain properties: Example 4.

Mesh	Matrix Elements	Fracture Elements
Mesh 1	5,222	812
Mesh 2	14,390	1,473
Mesh 3	23,126	2,189
Mesh 4	76,457	2,516

Table 8—Total number of matrix and fracture elements in different meshes used: Example 4.

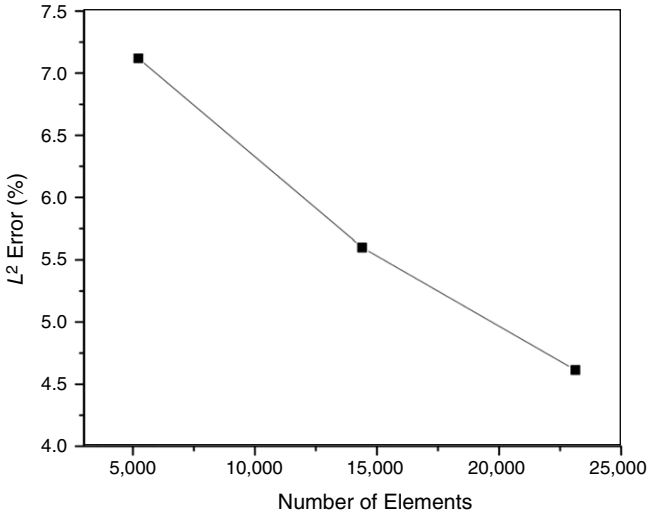

Fig. 12—Relative L^2 norm error: Example 4.

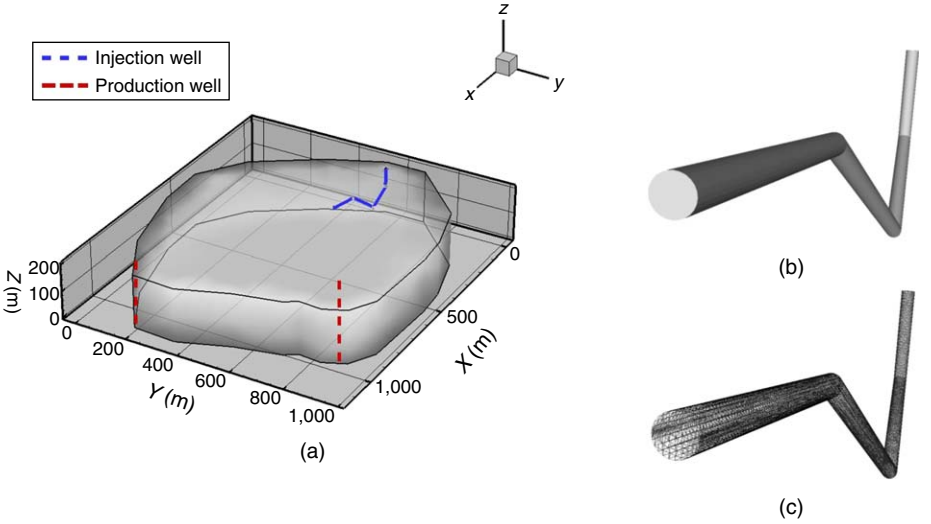

Fig. 13—(a) Domain geometry, (b) well geometry, and (c) well mesh: Example 5.

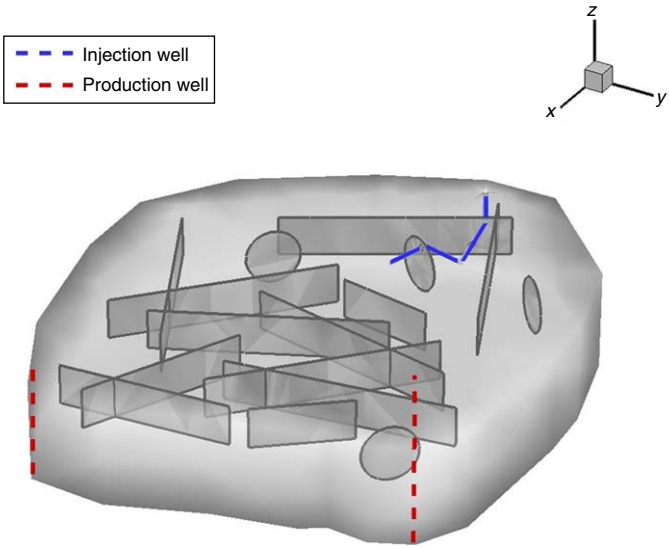

Fig. 14—Domain with fractures: Example 5.

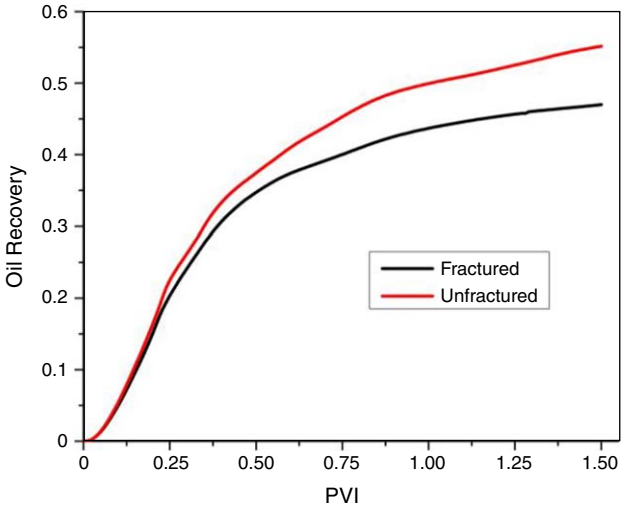

Fig. 15—Oil recovery with and without fractures: Example 5.

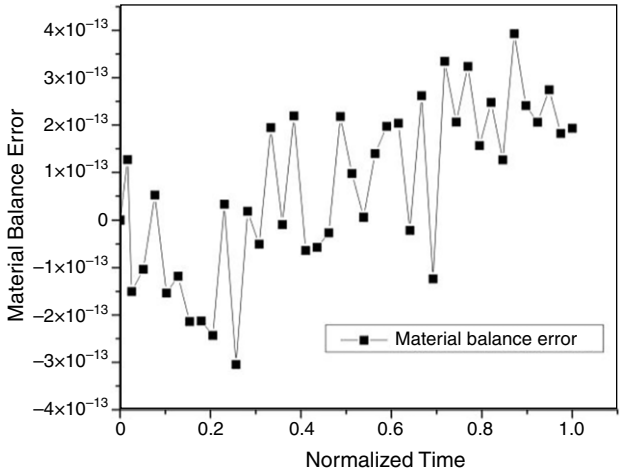

Fig. 16—Variation of material balance error during the simulation: Example 5.

Conclusions

This paper presents an efficient algorithm for compositional two-phase flow in fractured media with DWs. The model includes all commonly used types of FEs in 2D and 3D. The tools developed in the algorithm allow the generation of DWs in complex 3D geometries with fractures. This feature is a result of the interfaces that has been developed in the CAD framework and coupled to unstructured tetrahedrons. The proposed well discretization scheme preserves the shape of the well circumference at the expense of smaller girds in the immediate well vicinity. The fractures are readily set to impermeable faults due to the implementation of the flux calculation at the interfaces in 2D and 3D. The proposed algorithm is compared with different approaches with various degrees of complexity. Comparison with recent models in DFM and EDFM framework demonstrates the efficiency and accuracy of the proposed algorithm. The work presented in this paper has set the stage of extension to simulation of hydraulic and CO_2 fracturing.

Nomenclature

c = overall molar density of the mixture
C_t = total compressibility
c_α = molar density
E = grid edge
f_α = fractional flow function
F_i = sink/source term
$f_{\alpha,i}$ = fugacity
g = gas phase
$\mathbf{g}$ = gravitational acceleration
i = component index
$k_{r\alpha}$ = relative permeability
K = grid element
$\mathbf{K}$ = absolute permeability
n_c = number of components
$\boldsymbol{n}_E$ = outward normal vector
o = oil phase
p = pressure
$q_{K,E}$ = total flux across edge E in element K
$\overline{Q}_{\alpha,i}^{fr}$ = matrix–fracture exchange flux
T = temperature
$\boldsymbol{v}_\alpha$ = velocity of phase α
$\boldsymbol{v}_\alpha^{fr}$ = velocity across the fracture length
$\overline{V}_i$ = total partial molar volume
$x_{i,\alpha}$ = mole fraction
z_i = overall mole fraction
α = phase index
Δt = timestep
μ_α = dynamic viscosity
ρ_α = mass density
τ = simulation time
ϕ = porosity
$\phi_{K,j}$ = DG basis function
Ω = computational domain

Acknowledgment

This work was supported by the member companies of the Reservoir Engineering Research Institute (RERI) whose support is gratefully acknowledged.

References

Aavatsmark, I., Barkve, T., Boe, O. et al. 1998. Discretization on Unstructured Grids for Inhomogeneous, Anisotropic Media. Part I: Derivation of the Methods. *SIAM J Sci Comput* **19** (5): 1700–1716. https://doi.org/10.1137/S1064827595293582.

Aavatsmark, I., Eigestad, G. T., Heimsund, B. O. et al. 2010. A New Finite-Volume Approach to Efficient Discretization on Challenging Grids. *SPE J.* **15** (3): 658–669. SPE-106435-PA. https://doi.org/10.2118/106435-PA.

Abushaikhaa, A., Bluntb, M., Gosselinc, O. R. et al. 2015. Interface Control Volume Finite Element Method for Modelling Multi-Phase Fluid Flow in Highly Heterogeneous and Fractured Reservoirs. *J Comput Phys* **28:** 41–61. https://doi.org/10.1016/j.jcp.2015.05.024.

Ackerer, P. and Younes, A. 2008. Efficient Approximations for the Simulation of Density Driven Flow in Porous Media. *Adv Water Resour* **31** (1): 15–27. https://doi.org/10.1016/j.advwatres.2007.06.001.

Acs, G., Doleschall, S., and Farkas, E. 1985. General Purpose Compositional Model. *SPE J.* **25** (4): 543–553. SPE-10515-PA. https://doi.org/10.2118/10515-PA.

Ahmed, R., Edwards, M. G., Lamine, S. et al. 2015a. Control-Volume Distributed Multi-Point Flux Approximation Coupled with a Lower-Dimensional Fracture Model. *J Comput Phys* **284:** 462–489. https://doi.org/10.1016/j.jcp.2014.12.047.

Ahmed, R., Edwards, M. G., Lamine, S. et al. 2015b. Control-Volume Distributed Multi-Point Flux Approximation Coupled with a Lower-Dimensional Fracture Model. *J Comput Phys* **284:** 470–497. https://doi.org/10.1016/j.jcp.2014.12.047.

Amir S. Z. and Sun, S. 2017. An Efficient Two-Scale Hybrid Embedded Fracture Model for Shale Gas Simulation. *J Pet Sci Eng* **152:** 683–714. https://doi.org/10.1016/j.petrol.2016.12.023.

Artus, V., Fructus, D., and Houzé, O. 2017. Simulation of Deviated Wells Using 3D Unstructured Grids of Flexible Resolution. Paper presented at the SPE Reservoir Simulation Conference, Montgomery, Texas, USA, 20–22 February. SPE-182645-MS. https://doi.org/10.2118/182645-MS.

Aziz, K. and Settrai, A. 1979. *Petroleum Reservoir Simulation*. Bristol, UK: Applied Science Publishers.

Bahrainian, S. S. and Daneh, A. D. 2014. A Geometry-Based Adaptive Unstructured Grid Generation Algorithm for Complex Geological Media. *Comput Geosci* **68:** 31–37. https://doi.org/10.1016/j.cageo.2014.03.017.

Barenblatt, G., Zheltov, Y., and Kochina, I. 1960. Basic Concepts in the Theory of Seepage of Homogeneous Fluids in Fissurized Rocks. *J Appl Math Mech* **24** (5): 1286–1303. https://doi.org/10.1016/0021-8928(60)90107-6.

Barnea, D., Shoham, O., and Taitel, Y. 1985. Gas-Liquid Flow in Inclined Tubes: Flow Pattern Transitions for Upward Flow. *Chem Eng Sci* **40** (1): 131–136. https://doi.org/10.1016/0009-2509(85)85053-3.

Bastian, P., Helmig, R., Jakobs, H. et al. 2000. Numerical Simulation of Multiphase Flow in Fractured Porous Media. In *Numerical Treatment of Multiphase Flows in Porous Media*, ed. Z. Chen, R. Ewing, and Z.-C. Shi, Vol. 552, 1–18. Berlin, Germany: Lecture Notes in Physics, Springer-Verlag.

Beckner, B. L., Hutfilz, J. M., Ray, M. B. et al. 2001. EM: New Reservoir Simulation System. Paper presented at the SPE Middle East Oil Show, Bahrain, 17–20 March. SPE-68116-MS. https://doi.org/10.2118/68116-MS.

Beckner, B. L., Usadi, A. K., Ray, M. B. et al. 2006. Next Generation Reservoir Simulation Using Russian Linear Solvers. Paper presented at the SPE Russian Oil and Gas Technical Conference and Exhibition, Moscow, Russia, 3–6 October. SPE-103578-MS. https://doi.org/10.2118/103578-MS.

Beggs, D. H. and Brill, J. P. 1973. A Study of Two-Phase Flow in Inclined Pipes. *J Pet Technol* **25** (5): 607–617. SPE-4007-PA. https://doi.org/10.2118/4007-PA.

Bogdanov, I., Mourzenko, V., Thovert, J. et al. 2003. Two-Phase Flow through Fractured Porous Media. *Phys Rev E* **68** (2): 1–24. https://doi.org/10.1103/PhysRevE.68.026703.

Brezzi, F. and Fortin, M. 1991. *Mixed and Hybrid Finite Element Methods. Environmental Engineering*. New York, New York, USA: Springer-Verlag.

Chavent, G., Cohen, G., Jaffré, J. et al. 1990. Discontinuous and Mixed Finite Elements for Two-Phase Incompressible Flow. *SPE Res Eng* **5** (4): 567–575. SPE-16018-PA. https://doi.org/10.2118/16018-PA.

Chavent, G. and Jaffré, J. 1986. *Mathematical Models and Finite Elements for Reservoir Simulation. Studies in Mathematics and Its Applications*. North-Holland, The Netherlands: Elsevier.

Chavent, G. and Roberts, J. E. 1991. A Unified Physical Presentation of Mixed, Mixed-Hybrid Finite Element Method and Standard Finite Difference Approximations for the Determination of Velocities in Water Flow Problems. *Adv Water Resour* **14** (6): 329–348. https://doi.org/10.1016/0309-1708(91)90020-O.

Chen, J., Tiantai, L., and Zhang, Y. 2015. Application of the Unstructured Grids in the Numerical Simulation of Fractured Horizontal Wells in Ultra-Low Permeability Gas Reservoirs. *J Nat Gas Sci Eng* **22:** 580–590. https://doi.org/10.1016/j.jngse.2015.01.003.

Collins, D., Nghiem, L., Sharma, R. et al. 1992. Field-Scale Simulation of Horizontal Wells. *J Can Pet Technol* **31** (1): 21–9487. PETSOC-92-01-01. https://doi.org/10.2118/92-01-01.

Darlow, B., Ewing, R., and Wheeler, M. 1984. Mixed Finite Element Method for Miscible Displacement Problems in Porous Media. *SPE J*. **24** (4): 391–398. SPE-10501-PA. https://doi.org/10.2118/10501-PA.

Di Donato, G., Lu, H. Y., Taasoli, Z. et al. 2004. Multi-Rate-Transfer Dual-Porosity Modeling of Gravity Drainage and Imbibition. *SPE J*. **12** (1): 77–88. SPE-93144-PA. https://doi.org/10.2118/93144-PA.

Edwards, M. G. and Zheng, H. 2010. Quasi-Positive Families of Continuous Darcy-Flux Finite Volume Schemes on Structured and Unstructured Grids. *J Comput Appl Math* **234:** 2152–2161. https://doi.org/10.1016/j.cam.2009.08.078.

Escaron, P. C. 1983. A Technique To Evaluate Deviated Wells with Standard Logging Tools. Paper presented at the SPE Annual Technical Conference and Exhibition, San Francisco, California, USA, 5–8 October. SPE-12180-MS. https://doi.org/10.2118/12180-MS.

Firoozabadi, A. 2015. *Thermodynamics and Applications of Hydrocarbons Energy Production*. New York City, New York, USA: McGraw-Hill Professional.

Fung, L. S. K. and Du, S. 2016. Parallel-Simulator Framework for Multipermeability Modeling with Discrete Fractures for Unconventional and Tight Gas Reservoirs. *SPE J*. **21** (4): 1370–1385. SPE-179728-PA. https://doi.org/10.2118/179728-PA.

Geiger, S., Dentz, M., and Neuweiler, I. 2013. A Novel Multirate Dual-Porosity Model for Improved Simulation of Fractured and Multiporosity Reservoirs. *SPE J*. **18** (4): 670–684. SPE-148130-PA. https://doi.org/10.2118/148130-PA.

Geiger, S., Matthai, S., Niessner, J. et al. 2009. Black-Oil Simulations for Three-Component, Three-Phase Flow in Fractured Porous Media. *SPE J*. **14** (2): 338–354. SPE-107485-MS. https://doi.org/10.2118/107485-MS.

Geiger, S., Roberts, S., Matthai, S. et al. 2004. Combining Finite Element and Finite Volume Methods for Efficient Multiphase Flow Simulations in Highly Heterogeneous and Structurally Complex Geologic Media. *GeoFluids* **4** (4): 284–299. https://doi.org/10.1111/j.1468-8123.2004.00093.x.

Ghahri, P., Jamiolahmady, M., and Sohrabi, M. 2011. Gas Condensate Flow Around Deviated and Horizontal Wells. Paper presented at the SPE EUROPEC/EAGE Annual Conference and Exhibition, Vienna, Austria, 23–26 May. SPE-143577-MS. https://doi.org/10.2118/143577-MS.

Gilman, J. R. and Kazemi, H. 1983. Improvement in Simulation of Naturally Fractured Reservoirs. *SPE J*. **23** (4): 695–707. SPE-10511-PA. https://doi.org/10.2118/10511-PA.

Gouze, P., Borgne, L. and Leprovost, R. 2008. Non-Fickian Dispersion in Porous Media: 1. Multiscale Measurements Using Single Well Injection Withdrawal Tracer Tests at the Ses Sitjoles/Aliance Test Site (Spain). *Water Resour Res* **44** (6): W06426, 15 pages. https://doi.org/10.1029/2007WR006278.

Granet, S., Fabrie, P., Lemmonier, P. et al. 1998. A Single Phase Flow Simulation of Fractured Reservoir Using a Discrete Representation of Fractures. Paper Presented at the 6th European Conference on the Mathematics of Oil Recovery (ECMOR VI), Peebles, Scotland, UK, 8–11 September.

Haggerty, R. and Gorelick, S. M. 1995. Multiple-Rate Mass Transfer for Modelling Diffusion and Surface Reactions in Media with Pore-Scale Heterogeneity. *Water Resour Res* **31** (10): 2383–2400. https://doi.org/10.1029/95WR10583.

Hajibeygi, H., Karvounis, D., and Jenny, P. 2011. A Hierarchical Fracture Model for the Iterative Multiscale Finite Volume Method. *J Comput Phys* **230** (3): 628–643. https://doi.org/10.1016/j.jcp.2011.08.021.

Hasan, A. R. and Kabir, C. S. 1988. Predicting Multiphase Flow Behavior in a Deviated Well. *SPE Prod Eng* **3** (4): 474–482. SPE-15449-PA. https://doi.org/10.2118/15449-PA.

Heinemann, Z. E., Brand, C., Munka, M. et al. 1991. Modeling Reservoir Geometry with Irregular Grids. *SPE Res Eng* **6** (2): 225–232. SPE-18412-PA. https://doi.org/10.2118/18412-MS.

Hoteit, H., Ackerer, P., and Mosé, R. 2004. Nuclear Waste Disposal Simulations: Couplex Test Cases. *Comput Geosci* **8** (2): 99–124. https://doi.org/10.1023/B:COMG.0000035074.37722.71.

Hoteit H. and Firoozabadi, A. 2005. Multicomponent Fluid Flow by Discontinuous Galerkin and Mixed Methods in Unfractured and Fractured Media. *Water Resour Res* **41** (11): W11412, 15 pages. https://doi.org/10.1029/2005WR004339.

Hoteit, H. and Firoozabadi, A. 2008. An Efficient Model for Incompressible Two-Phase Flow in Fractured Media. *Adv Water Resour* **31:** 891–905. https://doi.org/10.1016/j.advwatres.2008.02.004.

Huggenberger, P., Zidane, A., Zechner, E. et al. 2015. The Role of Tectonic Structures and Density-Driven Groundwater Flow for Salt Karst Formation. *Eng Geol Society Territ* **5:** 609–612. https://doi.org/10.1007/978-3-319-09048-1_118.

Hui, M.-H., Karimi-Fard, M., Mallison, B. et al. 2018. A General Modeling Framework for Simulating Complex Recovery Processes in Fractured Reservoirs at Different Resolutions. Paper presented at the SPE Reservoir Simulation Conference, Montgomery, Texas, USA, 20–22 February. SPE-182621-PA. https://doi.org/10.2118/182621-PA.

Hyman, J. D., Karra, S., Makedonska N. et al. 2015. DFNWORKS: A Discrete Fracture Network Frame Work for Modeling Subsurface Flow and Transport. *Comput Geosci* **84:** 10–19. https://doi.org/10.1016/j.cageo.2015.08.001.

Intel Core is a trademark of Intel Corporation or its subsidiaries, 2200 Mission College Boulevard, Santa Clara, California 95052, USA.

Jiang, J. and Younis, R. M. 2016. Hybrid Coupled Discrete-Fracture/Matrix and Multicontinuum Models for Unconventional-Reservoir Simulation. *SPE J*. **21** (3): 1009–1027. SPE-178430-PA. https://doi.org/10.2118/178430-PA.

Karimi-Fard, M., Durlofsky, L. J., and Aziz, K. 2004. An Efficient Discrete-Fracture Model Applicable for General Purpose Reservoir Simulators. *SPE J*. **9** (2): 227–236. SPE-88812-PA. https://doi.org/10.2118/88812-PA.

Karypis, G. and Kumar, V. 1998. *METIS 4.0: Unstructured Graph Partitioning and Sparse Matrix Ordering System*. Technical Report, University of Minnesota, Minneapolis, Minnesota, USA.

Kazemi, H. and Gilman, J. 1969. Pressure Transient Analysis of Naturally Fractured Reservoirs with Uniform Fracture Distribution. *SPE J*. **9** (4): 451–462. SPE-2156-A. https://doi.org/10.2118/2156-A.

Kazemi, H. and Gilman, J. 1992. Analytical and Numerical Solution of Oil Recovery from Fractured Reservoirs with Empirical Transfer Functions. *SPE J*. **7** (2): 219–227. SPE-19849-PA. https://doi.org/10.2118/19849-PA.

Kazemi, H. and Merrill, L. 1979. Numerical Simulation of Water Imbibition in Fractured Cores. *SPE J*. **19** (3): 175–182. SPE-6895-PA. https://doi.org/10.2118/6895-PA.

Kazemi, H., Merrill, L. S., Porterfield, K. L. et al. 1976. Numerical Simulation of Water-Oil Flow in Naturally Fractured Reservoirs. *SPE J*. **16** (6): 317–326. SPE-5719-PA. https://doi.org/10.2118/5719-PA.

Kim, J. G. and Deo, M. D. 2000. Finite-Element, Discrete-Fracture Model for Multiphase Flow in Porous Media. *AIChE J* **46** (6): 1120–1130. https://doi.org/10.1002/aic.690460604.

Kruger, C. 2007. The Challenges of Deviated Wells. Paper presented at the SPE/IADC Middle East Drilling and Technology Conference, Cairo, Egypt, 22–24 October. SPE-108270-MS. https://doi.org/10.2118/108270-MS.

Lamine, S. and Edwards, M. G. 2010. Multidimensional Upwind Convection Schemes for Flow in Porous Media on Structured and Unstructured Quadrilateral Grids. *J Comput Appl Math* **234:** 2106–2117. https://doi.org/10.1016/j.cam.2009.08.069.

Lee, S. H., Lough, M. F., and Jensen, C. L. 2001. Hierarchical Modeling of Flow in Naturally Fractured Formations with Multiple Length Scales. *Water Resour Res* **37** (3): 443–455. https://doi.org/10.1029/2000WR900340.

Li, L. and Lee, S. H. 2008. Efficient Field-Scale Simulation of Black Oil in a Naturally Fractured Reservoir through Discrete Fracture Networks and Homogenized Media. *SPE Res Eval & Eng* **11** (4): 1094–6470. SPE-103901-PA. https://doi.org/10.2118/103901-PA.

Li, Z. and Firoozabadi, A. 2012. Initialization of Phase Fractions in Rachford-Rice Equations for Robust and Efficient Three-Phase Split Calculation. *Fluid Phase Equilib* **332:** 21–27. https://doi.org/10.1016/j.cam.2009.08.069.

Liu, K., Subramanian, G., Dratler, D. I. et al. 2009. A General Unstructured-Grid, Equation-of-State-Based, Fully Implicit Thermal Simulator for Complex Reservoir Processes. *SPE J*. **14** (2): 355–361. SPE-106073-PA. https://doi.org/10.2118/106073-PA.

Lohrenz, J., Bray, B. G., and Clark, C. R. 1964. Calculating Viscosities of Reservoir Fluids from Their Compositions. *J Pet Technol* **16** (10): 1171–1176. SPE-915-PA. https://doi.org/10.2118/915-PA.

Lu, H., Di Donato, G., and Blunt, M. J. 2008. General Transfer Functions for Multiphase Flow in Fractured Reservoirs. *SPE J*. **13** (3): 289–297. SPE-102542-PA. https://doi.org/10.2118/102542-PA.

Makedonska, N., Painter, S. L., Bui, Q. M. et al. 2015. Particle Tracking Approach for Transport in Three-Dimensional Discrete Fracture Networks. *J Comput Geosci* **19:** 1123–1137. https://doi.org/10.1007/s10596-015-9525-4.

Martin, V., Jaffre, J., and Roberts, J. 2005. Modeling Fractures and Barriers as Interfaces for Flow in Porous Media. *SIAM J Sci Comput* **26** (5): 1667–1691. https://doi.org/10.1137/S1064827503429363.

Matthai, S. K., Geiger, S., Roberts, S. G. et al. 2007a. *Numerical Simulation of Multiphase Fluid Flow in Structurally Complex Reservoirs*, 405–429. London, UK: Special Publications 292, Geological Society.

Matthai, S. K., Mezentsev, A., and Belayneh, M. 2007b. Finite Element Node-Centered Finite-Volume Experiments with Fractured Rock Represented by Unstructured Hybrid Element Meshes. *SPE Res Eval & Eng* **10** (6): 740–756. SPE-93341-PA. https://doi.org/10.2118/93341-PA.

Moinfar, A., Varavei, A., Sepehrnoori, K. et al. 2014. Development of an Efficient Embedded Discrete Fracture Model for 3D Compositional Reservoir Simulation in Fractured Reservoirs. *SPE J*. **19** (2): 289–303. SPE-154246-PA. https://doi.org/10.2118/154246-PA.

Moortgat, J. and Firoozabadi, A. 2016. Mixed-Hybrid and Vertex-Discontinuous-Galerkin Finite Element Modeling of Multiphase Compositional Flow on 3D Unstructured Grids. *J Comput Phys* **315:** 476–500. https://doi.org/10.1016/j.jcp.2016.03.054.

Mosé, R., Siegel, P., Ackerer, P. et al. 1994. Application of the Mixed Hybrid Finite Element Approximation in a Ground Water Flow Model: Luxury or Necessity? *Water Resour Res* **30** (11): 3001–3012. https://doi.org/10.1029/94WR01786.

Naccache, P. F. 1997. A Fully-Implicit Thermal Reservoir Simulator. Paper Presented at the SPE Reservoir Simulation Symposium, Dallas, Texas, USA, 8–11 June. SPE-37985-MS. https://doi.org/10.2118/37985-MS.

Nejati, M., Paluszny, A., and Zimmerman, R. W. 2015. On the Use of Quarter-Point Tetrahedral Finite Elements in Linear Elastic Fracture Mechanics. *Eng Fract Mech* **144:** 194–221. https://doi.org/10.1016/j.engfracmech.2015.06.055.

Nghiem, L. X., Sharma, R., Collins, D. A. et al. 1992. Simulation of Horizontal and Deviated Wells in Naturally Fractured Reservoirs. Paper presented at the Annual Technical Meeting, Calgary, Alberta, June 7–10. PETSOC-92-15. https://doi.org/10.2118/92-15.

Nick, H. M. and Matthai, S. K. 2011. Comparison of Three FE-FV Numerical Schemes for Single- and Two-Phase Flow Simulation of Fractured Porous Media. *Transp Porous Media* **90:** 421–444. https://doi.org/10.1007/s11242-011-9793-y.

Noorishad, J. and Mehran, M. 1982. An Upstream Finite Element Method for Solution of Transient Transport Equation in Fractured Porous Media. *Water Resour Res* **18** (3):588–596. https://doi.org/10.1029/WR018i003p00588.

Ozkaya, S. I. 2017. Modeling Finite-Fracture Networks in a Partially Fractured Reservoir in the Middle East. *SPE Res Eval & Eng* **20** (4): 1094–6470. SPE-185171-PA. https://doi.org/10.2118/185171-PA.

Peng, D. Y. and Robinson, D. B. 1976. A New Two-Constant Equation of State. *Ind Eng Chem Fundam* **15:** 59–64. https://doi.org/10.1021/i160057a011.

Quandalle, P. and Sabathier, J. C. 1989. Typical Features of a Multipurpose Reservoir Simulator. *SPE Res Eng* **4** (4): 475–480. SPE-16007-PA. https://doi.org/10.2118/16007-PA.

Reichenberger, V., Jakobs H., Bastian P. et al. 2006. A Mixed-Dimensional Finite Volume Method for Multiphase Flow in Fractured Porous Media. *Adv Water Res* **29:** 1030–1036. https://doi.org/10.1016/j.advwatres.2005.09.001.

Reiter, S., Logashenko, D., Grillo, A. et al. 2012. Preparation of Grids for Simulations of Groundwater Flow in Fractured Porous Media. *Comput Visual Sci* **15:** 209–225. https://doi.org/10.1007/s00791-013-0210-7.

Sanchez, N., Marin, A., and Rattia, A. 1992. Simulation of a Highly Deviated Well in a Naturally Fractured Reservoir, Lake Maracaibo, Venezuela. Paper presented at the SPE Latin America Petroleum Engineering Conference, Caracas, Venezuela, 8–11 March. SPE-23614-MS. https://doi.org/10.2118/23614-MS.

Sandve, T. H., Berre, I., and Nordbotten, J. M. 2012. An Efficient Multi-Point Flux Approximation Method for Discrete Fracture–Matrix Simulations. *J Comput Phys* **231:** 3784–3800. https://doi.org/10.1016/j.jcp.2012.01.023.

Sarda, S., Jeannin, L., Basquet, R. et al. 2002. Hydraulic Characterization of Fractured Reservoirs: Simulation on Discrete Fracture Models. *SPE Res Eval & Eng* **5** (2): 154–162. SPE-77300-PA. https://doi.org/10.2118/77300-PA.

Schmid, K. S., Geiger, S., and Sorbie K. S. 2013. Higher Order FE–FV Method on Unstructured Grids for Transport and Two-Phase Flow with Variable Viscosity in Heterogeneous Porous Media. *J Comput Phys* **241:** 416–444. https://doi.org/10.1016/j.jcp.2012.12.017.

Si, H. 2011. TetGen: A Quality Tetrahedral Mesh Generator and a 3D Delaunay Triangulator. http://wias-berlin.de/software/tetgen/ (accessed 6 December 2019).

Stanlsav, J. F., Christensen, K., and Chakma, A. 1990. Two Phase Flow in Highly Deviated Wells. Paper presented at the Annual Technical Meeting, Calgary, Alberta, Canada, 10–13 June. PETSOC-90-70. https://doi.org/10.2118/90-70.

Tang, C., Chen, X., Du, Z. et al. 2018. Numerical Simulation Study on Seepage Theory of a Multi-Section Fractured Horizontal Well in Shale Gas Reservoirs Based on Multi-Scale Flow Mechanisms. *Energies* **11** (9): 2329. https://doi.org/10.3390/en11092329.

Tene, M., Sebastian, B. M. B., Al Kobaisi, M. S. et al. 2017. Projection-Based Embedded Discrete Fracture Model (pEDFM). *Adv Water Resour* **105:** 205–216. https://doi.org/10.1016/j.advwatres.2017.05.009.

Thomas, L., Dixon T., and Pierson R. 1983. Fractured Reservoir Simulation. *SPE J.* **23** (1): 42–54. SPE-9305-PA. https://doi.org/10.2118/9305-PA.

Unsal, E., Stephan, K., Matthai, S. K. et al. 2010. Simulation of Multiphase Flow in Fractured Reservoirs Using a Fracture-Only Model with Transfer Functions. *Comput Geosci* **14** (4): 527–538. https://doi.org/10.1007/s10596-009-9168-4.

Usadi, A., Mishev, I., Shaw, J. et al. 2007. Parallelization on Unstructured Grids. Paper presented at the SPE Reservoir Simulation Symposium, Houston, Texas, USA. SPE-106063-MS. https://doi.org/10.2118/106063-MS.

Warren, J. and Root, P. 1963. The Behavior of Naturally Fractured Reservoirs. *SPE J.* **3** (3): 245–255. SPE-426-PA. https://doi.org/10.2118/426-PA.

Watts, J. W. 1986. A Compositional Formulation of the Pressure and Saturation Equations. *SPE Res Eng* **1** (3): 243–252. SPE-12244-PA. https://doi.org/10.2118/12244-PA.

Weirong, L., Zhenzhen, D., and Gang, L. 2017. Integrating Embedded Discrete Fracture and Dual-Porosity, Dual-Permeability Methods to Simulate Fluid Flow in Shale Oil Reservoirs. *Energies* **10** (10): 1471. https://doi.org/10.3390/en10101471.

Yan, X., Huang, Z., Yao, J. et al. 2016. An Efficient Embedded Discrete Fracture Model Based on Mimetic Finite Difference Method. *J Pet Sci Eng* **145:** 11–21. https://doi.org/10.1016/j.petrol.2016.03.013.

Younes, A., Fahs, M., and Belfort, B. 2013. Monotonicity of the Cell-Centred Triangular MPFA Method for Saturated and Unsaturated Flow in Heterogeneous Porous Media. *J Hydrol* **504:** 132–141. https://doi.org/10.1016/j.jhydrol.2013.09.041.

Younes, A., Fahs, M., Zidane, A. et al. 2015. A New Benchmark with High Accurate Solution for Hot–Cold Fluids Mixing. *Heat Mass Transfer* **51** (9): 1321–1336. https://doi.org/10.1007/s00231-015-1500-z.

Younes, A., Konz, M., Fahs, M. et al. 2011. Modelling Variable Density Flow Problems in Heterogeneous Porous Media Using the Method of Lines and Advanced Spatial Discretization Methods. *Math Comput Simul* **81:** 2346–2355. https://doi.org/10.1016/j.matcom.2011.02.010.

Younes, A., Markadi, A., Zidane, A. et al. 2014. A Combination of Crouzeix-Raviart, Discontinuous Galerkin and MPFA Methods for Buoyancy-Driven Flows. *Int J Num Methods Heat Fluid Flow* **24** (3): 735–759. https://doi.org/10.1108/HFF-07-2012-0156.

Yu, W., Xu, Y., Weijermars, R. et al. 2017. A Numerical Model for Simulating Pressure Response of Well Interference and Well Performance in Tight Oil Reservoirs with Complex-Fracture Geometries Using the Fast Embedded-Discrete-Fracture-Model Method. *SPE Res Eval & Eng* **21** (2): 489–502. SPE-184825-PA. https://doi.org/10.2118/184825-PA.

Zidane, A. and Firoozabadi, A. 2014. An Efficient Numerical Model for Multicomponent Compressible Flow in Fractured Porous Media. *Adv Water Resour* **74:** 127–147. https://doi.org/10.1016/j.advwatres.2014.08.010.

Zidane, A. and Firoozabadi, A. 2015. An Implicit Numerical Model for Multicomponent Compressible Two-Phase Flow in Porous Media. *Adv Water Resour* **85:** 64–78. https://doi.org/10.1016/j.advwatres.2015.09.006.

Zidane, A. and Firoozabadi, A. 2017. Fracture-Cross-Flow Equilibrium in Compositional Two-Phase Reservoir Simulation. *SPE J.* **22** (3): 950–970. SPE-184402-PA. https://doi.org/10.2118/184402-PA.

Zidane, A. and Firoozabadi, A. 2018a. Reservoir Simulation of Fractured Media in Compressible Single-Phase Multicomponent in 2D, 2.5D, and 3D Unstructured Gridding. *Adv Water Resour* **121:** 68–96. https://doi.org/10.1016/j.advwatres.2018.08.005.

Zidane, A. and Firoozabadi, A. 2018b. Efficient Simulation of Two-Phase Compositional Flow in Fractured Reservoirs Using 3D Unstructured Gridding in Complex Geometries. Paper presented at the SPE Annual Technical Conference and Exhibition, Dallas, Texas, USA, 24–26 September. SPE-191405-MS. https://doi.org/10.2118/191405-MS.

Zidane, A., Younes, A., Huggenberger, P. et al. 2012. The Henry Semi-Analytical Solution for Saltwater Intrusion with Reduced Dispersion. *Water Resour Res* **48:** 6533. https://doi.org/10.1029/2011WR011157.

Zidane, A., Zechner, E., Huggenberger, P. et al. 2014a. On the Effects of Subsurface Parameters on Evaporite Dissolution (Switzerland). *J Contamin Hydrol* **160:** 42–52. https://doi.org/10.1016/j.jconhyd.2014.02.006.

Zidane, A., Zechner, E., Huggenberger, P. et al. 2014b. Simulation of Rock Salt Dissolution and Its Impact on Land Subsidence. *Hydrol Earth Sys Sci* **18:** 2177–2189. https://doi.org/10.5194/hess-18-2177-2014.

Appendix A: Well Implementation

Well implementation in our model is by fully unstructured grids. As opposed to prismatic and Voronoi grids, unstructured tetrahedra can readily describe complex geometries in 3D. One restriction that the well imposes on the simulation model relates to the computational time. Well diameter could be in the range of few centimeters, when the reservoir is in kilometer scale. Because of the Courant–Freidrich–Levy (CFL) condition, the size of timestep is, therefore, restricted by the small elements in the immediate well vicinity. The size of matrix grids near the well region is ensured to be at their maximum allowed size honoring the Delaunay tetrahedralizations. Coarsening the well geometry allows for larger matrix elements near the well region; however, it affects the well meanders. The well effect in terms of injection/production is accounted for in the simulation through the boundaries of the well elements that are in contact with the simulation domain. The well elements are not included in the simulation. When matching the interfaces of the well elements with the matrix domain, the traces of the pressure are, therefore, evaluated by the MHFE method. Fluxes at the matrix/well interfaces are treated as boundary condition flux. Imposing the boundary condition at the well/matrix boundary is made possible because well elements are not part of the simulation domain.

The well with its inclination is first designed in a CAD platform (**Fig. A-1a**) and then discretized with unstructured tetrahedra (Fig. A-1b shows cross section of the well with unstructured tetrahedra). The size of matrix finite elements discretized without the well is kept large (Fig. A-1c), and the accuracy is guaranteed by the higher-order discretization. When including the well, the mesh is gradually refined near the well region (Fig. A-1d). The triangular interfaces of the tetrahedra elements in the matrix domain should match the interfaces of the well elements at the same coordinates. In the last step, the well elements are removed from the original mesh, and the final mesh is then ready for simulation. We note that with this procedure, the effect of the well in the simulation is included by the interfaces that match the well wall, and the well rate is distributed along the total number of interfaces for elements at the well–matrix boundary. In our future investigation in well modeling, the well hydraulics will be taken into consideration.

One advantage of our well modeling approach is the ease to change/adapt the mesh size at the well location. A deviated well requires more refinement to capture the deviation meanders. With higher refinement, the CPU time is increased for two reasons: (i) the CFL condition in the matrix domain and (ii) the overall increase in the total number of elements to preserve the well details. To overcome this limitation, our modeling technique allows using large elements at the well location. Depending on the type of simulation, a tradeoff should be made between well shape and efficiency. The proposed modeling technique allows to choose a different order of refinement/coarsening. To demonstrate this capability, we show in **Fig. A-2** the mesh in discretization of the well discussed earlier and in **Fig. A-3** different refinements for the same well. Fig. A-3 reveals that the coarser the grids are at the well, the more of its meander details are lost.

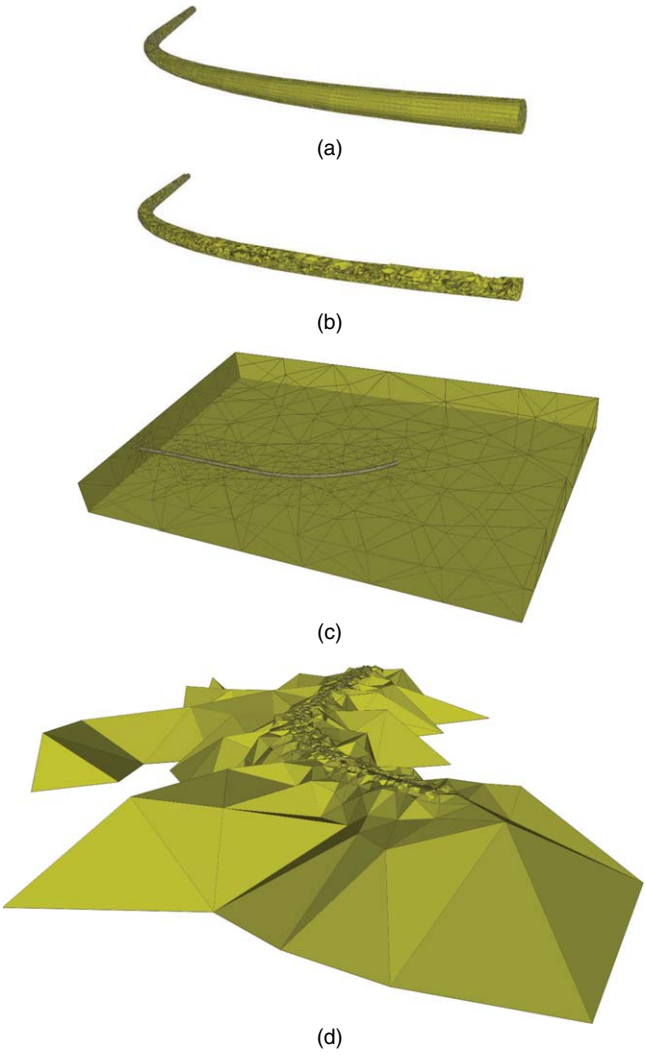

Fig. A-1—(a and b) Discretization mesh of well, size enlarged for clarity; (c) reservoir with the well; and (d) reservoir grids near the well.

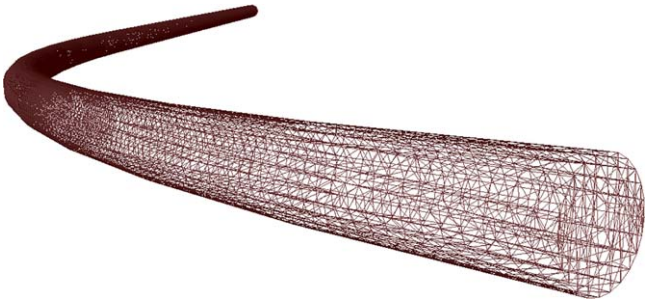

Fig. A-2—Well discretization mesh.

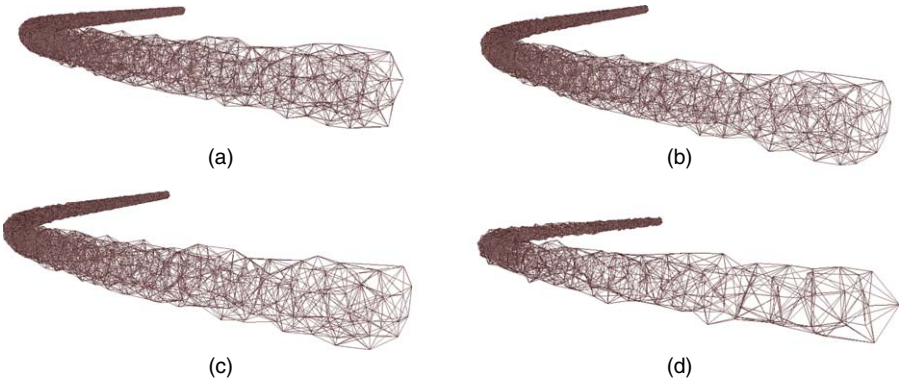

Fig. A-3—Different coarsening levels for the well from (a) the finer mesh to (d) the coarse mesh.

Appendix B: Fractures Anisotropy

One of the features in our model is the ease to assign anisotropic permeability across the normal and lateral sides of the fractures. To demonstrate this ability, we rerun the simulation of Example 1 in the text by having a normal permeability value of the fractures to be two orders of magnitude less compared with the lateral side. Note that the fractures are represented by $(n-1)-D$ in our algorithm; therefore, having low permeability across the normal side reduces the matrix–fracture exchange significantly. This is due to the negligible flow from the fracture interface ($(n-2)-D$) to the matrix domain ($n-D$). For reference, we show in **Fig. B-1** the gas saturation at 60% PVI for the problem discussed in Example 1 in the text and with the permeability values discussed above.

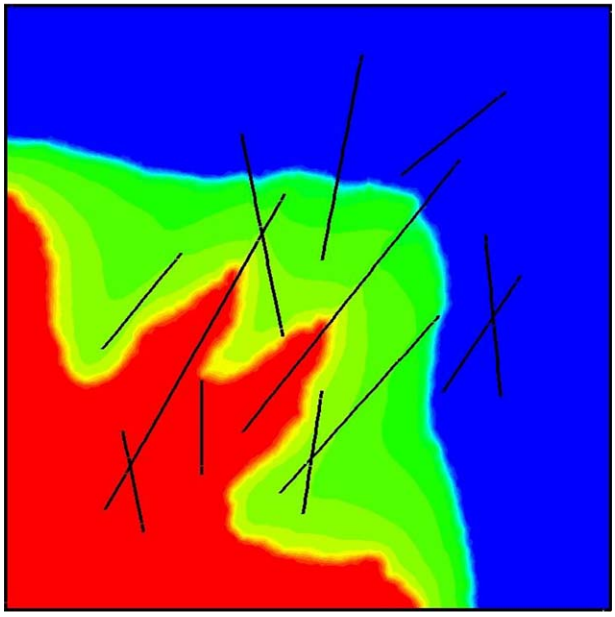

Fig. B-1—Gas saturation at 60% PVI for anisotropic permeability in the fractures: Example 1 in the text.

Appendix C: Fracture and Impermeable Fault Coordinates

In the following, we provide geometric coordinates in feet for all fractures and impermeable faults of Example 3 in the text. **Table C-1** shows the starting and end coordinates for all fractures and impermeable faults. Note that the fractures are vertical extending from top to bottom of the domain.

X_start	Y_start	X_end	Y_end	Description	X_start	Y_start	X_end	Y_end	Description
755.58	55.78	801.63	25.81	Fracture	767.67	598.84	938.23	882.01	Impermeable fault
688.89	21.6	755.58	55.78	Fracture	642.23	698.87	837.24	771.94	Impermeable fault
755.58	55.78	802.03	79.58	Fracture	27.54	824.82	88.58	706.52	Impermeable fault
495.28	796.57	565.59	876.43	Fracture	37.71	559.58	146.84	731.48	Impermeable fault
588.77	840.43	638.87	863.93	Fracture	47.68	507.43	393.8	470.65	Impermeable fault
638.87	863.93	840.74	958.63	Fracture	423.99	246.72	531.34	393.17	Impermeable fault

Table C-1—Geometric coordinates in feet for all fractures and faults in Example 3.

X_start	Y_start	X_end	Y_end	Description	X_start	Y_start	X_end	Y_end	Description
549.15	921.76	583.76	889.61	Fracture	557.93	227.59	875.82	296.65	Impermeable fault
583.76	889.61	614.3	861.24	Fracture	737.61	239.56	872.13	180.63	Impermeable fault
583.76	889.61	603.29	897.9	Fracture	402.08	982.71	792.78	953.69	Impermeable fault
589.29	911.27	603.29	897.9	Fracture	375.34	12.83	499.74	80.95	Impermeable fault
603.29	897.9	638.87	863.93	Fracture	957.05	23.55	932.93	251.1	Impermeable fault
638.87	863.93	685.23	819.66	Fracture	28.97	54.44	56.23	205.29	Impermeable fault
55.11	913.42	175.86	969.41	Fracture	636.61	913.1	719.2	947.12	Fracture
175.86	969.41	220.14	909.81	Fracture	627.05	774.27	685.23	819.66	Fracture
220.14	909.81	250.21	925.55	Fracture	95.28	546.57	165.59	626.43	Fracture
229.36	946.34	250.21	925.55	Fracture	188.77	590.43	238.87	613.93	Fracture
250.21	925.55	287.8	888.06	Fracture	238.87	613.93	440.74	708.63	Fracture
250.21	925.55	288.88	945.78	Fracture	149.15	671.76	183.76	639.61	Fracture
288.88	945.78	337.95	971.46	Fracture	183.76	639.61	214.3	611.24	Fracture
288.88	945.78	330.7	894.05	Fracture	183.76	639.61	203.29	647.9	Fracture
81.28	871.25	100.44	881.14	Fracture	189.29	661.27	203.29	647.9	Fracture
100.44	881.14	138.88	804.12	Fracture	203.29	647.9	238.87	613.93	Fracture
100.44	881.14	166.41	915.18	Fracture	238.87	613.93	285.23	569.66	Fracture
142.83	931.04	166.41	915.18	Fracture	165.59	626.43	188.77	590.43	Fracture
166.41	915.18	267.73	847.08	Fracture	188.77	590.43	206.09	563.53	Fracture
267.73	847.08	296.95	827.43	Fracture	129.26	532.29	206.09	563.53	Fracture
296.95	827.43	164.1	779.45	Fracture	206.09	563.53	257.14	584.29	Fracture
267.73	847.08	376.91	914.58	Fracture	227.05	524.27	319.1	562.23	Fracture
320.05	828.91	355.58	805.78	Fracture	319.1	562.23	459.62	620.18	Fracture
355.58	805.78	401.63	775.81	Fracture	272.55	608.63	319.1	562.23	Fracture
288.89	771.6	355.58	805.78	Fracture	319.1	562.23	332.31	549.06	Fracture
355.58	805.78	402.03	829.58	Fracture	201.41	690.98	236.61	663.1	Fracture
404.98	867.17	518.12	925.15	Fracture	236.61	663.1	271.82	635.21	Fracture
455.11	663.42	575.86	719.41	Fracture	236.61	663.1	319.2	697.12	Fracture
575.86	719.41	620.14	659.81	Fracture	227.05	524.27	285.23	569.66	Fracture
620.14	659.81	650.21	675.55	Fracture	495.28	296.57	565.59	376.43	Fracture
629.36	696.34	650.21	675.55	Fracture	588.77	340.43	638.87	363.93	Fracture
650.21	675.55	687.8	638.06	Fracture	638.87	363.93	840.74	458.63	Fracture
650.21	675.55	688.88	695.78	Fracture	549.15	421.76	583.76	389.61	Fracture
688.88	695.78	737.95	721.46	Fracture	583.76	389.61	614.3	361.24	Fracture
688.88	695.78	730.7	644.05	Fracture	583.76	389.61	603.29	397.9	Fracture
481.28	621.25	500.44	631.14	Fracture	589.29	411.27	603.29	397.9	Fracture
500.44	631.14	538.88	554.12	Fracture	603.29	397.9	638.87	363.93	Fracture
500.44	631.14	566.41	665.18	Fracture	638.87	363.93	685.23	319.66	Fracture
542.83	681.04	566.41	665.18	Fracture	565.59	376.43	588.77	340.43	Fracture
566.41	665.18	667.73	597.08	Fracture	588.77	340.43	606.09	313.53	Fracture
667.73	597.08	696.95	577.43	Fracture	529.26	282.29	606.09	313.53	Fracture
696.95	577.43	564.1	529.45	Fracture	606.09	313.53	657.14	334.29	Fracture
667.73	597.08	776.91	664.58	Fracture	627.05	274.27	719.1	312.23	Fracture
720.05	578.91	755.58	555.78	Fracture	719.1	312.23	859.62	370.18	Fracture
755.58	555.78	801.63	525.81	Fracture	672.55	358.63	719.1	312.23	Fracture
688.89	521.6	755.58	555.78	Fracture	719.1	312.23	732.31	299.06	Fracture
755.58	555.78	802.03	579.58	Fracture	601.41	440.98	636.61	413.1	Fracture
55.11	413.42	175.86	469.41	Fracture	636.61	413.1	671.82	385.21	Fracture
175.86	469.41	220.14	409.81	Fracture	636.61	413.1	719.2	447.12	Fracture
220.14	409.81	250.21	425.55	Fracture	627.05	274.27	685.23	319.66	Fracture
229.36	446.34	250.21	425.55	Fracture	95.28	46.57	165.59	126.43	Fracture
250.21	425.55	287.8	388.06	Fracture	188.77	90.43	238.87	113.93	Fracture

Table C-1 (continued)—Geometric coordinates in feet for all fractures and faults in Example 3.

X_start	Y_start	X_end	Y_end	Description	X_start	Y_start	X_end	Y_end	Description
250.21	425.55	288.88	445.78	Fracture	238.87	113.93	440.74	208.63	Fracture
288.88	445.78	337.95	471.46	Fracture	149.15	171.76	183.76	139.61	Fracture
288.88	445.78	330.7	394.05	Fracture	183.76	139.61	214.3	111.24	Fracture
81.28	371.25	100.44	381.14	Fracture	183.76	139.61	203.29	147.9	Fracture
100.44	381.14	138.88	304.12	Fracture	189.29	161.27	203.29	147.9	Fracture
100.44	381.14	166.41	415.18	Fracture	203.29	147.9	238.87	113.93	Fracture
142.83	431.04	166.41	415.18	Fracture	238.87	113.93	285.23	69.66	Fracture
166.41	415.18	267.73	347.08	Fracture	165.59	126.43	188.77	90.43	Fracture
267.73	347.08	296.95	327.43	Fracture	188.77	90.43	206.09	63.53	Fracture
296.95	327.43	164.1	279.45	Fracture	129.26	32.29	206.09	63.53	Fracture
267.73	347.08	376.91	414.58	Fracture	206.09	63.53	257.14	84.29	Fracture
320.05	328.91	355.58	305.78	Fracture	227.05	24.27	319.1	62.23	Fracture
355.58	305.78	401.63	275.81	Fracture	319.1	62.23	459.62	120.18	Fracture
288.89	271.6	355.58	305.78	Fracture	272.55	108.63	319.1	62.23	Fracture
355.58	305.78	402.03	329.58	Fracture	319.1	62.23	332.31	49.06	Fracture
455.11	163.42	575.86	219.41	Fracture	201.41	190.98	236.61	163.1	Fracture
575.86	219.41	620.14	159.81	Fracture	236.61	163.1	271.82	135.21	Fracture
620.14	159.81	650.21	175.55	Fracture	236.61	163.1	319.2	197.12	Fracture
629.36	196.34	650.21	175.55	Fracture	227.05	24.27	285.23	69.66	Fracture
650.21	175.55	687.8	138.06	Fracture	956.58	869.25	876.47	559.61	Fracture
650.21	175.55	688.88	195.78	Fracture	876.47	559.61	865.48	517.11	Fracture
688.88	195.78	737.95	221.46	Fracture	853.3	648.14	876.47	559.61	Fracture
688.88	195.78	730.7	144.05	Fracture	876.47	559.61	935.44	334.26	Fracture
481.28	121.25	500.44	131.14	Fracture	935.44	334.26	954.06	263.11	Fracture
500.44	131.14	538.88	54.12	Fracture	954.06	397.59	935.44	334.26	Fracture
500.44	131.14	566.41	165.18	Fracture	935.44	334.26	847.09	33.79	Fracture
542.83	181.04	566.41	165.18	Fracture	355.93	418.06	755.45	486.22	Fracture
566.41	165.18	667.73	97.08	Fracture	56.06	249.97	501.12	210.17	Fracture
667.73	97.08	696.95	77.43	Fracture	440.74	708.63	459.62	620.18	Fracture
696.95	77.43	564.1	29.45	Fracture	459.62	620.18	461.61	500.18	Fracture
667.73	97.08	776.91	164.58	Fracture	182.49	710	519.3	725	Fracture
720.05	78.91	755.58	55.78	Fracture	355.93	428.06	755.45	486.22	Fracture
565.59	876.43	588.77	840.43	Fracture	110.04	67.01	88.37	212.98	Impermeable fault
588.77	840.43	606.09	813.53	Fracture	121.22	226.95	196	163.39	Impermeable fault
529.26	782.29	606.09	813.53	Fracture	19.49	278.62	56.45	465.52	Impermeable fault
606.09	813.53	657.14	834.29	Fracture	401.1	454.12	727.16	490.17	Impermeable fault
627.05	774.27	719.1	812.23	Fracture	448.72	571.74	309.25	501.69	Impermeable fault
719.1	812.23	859.62	870.18	Fracture	477.63	571.74	570.85	488.69	Impermeable fault
672.55	858.63	719.1	812.23	Fracture	839.99	488.88	909.46	334.11	Impermeable fault
719.1	812.23	732.31	799.06	Fracture	947.12	466.44	984.7	828.33	Impermeable fault
601.41	940.98	636.61	913.1	Fracture	786.95	856.7	910.72	929.03	Impermeable fault
636.61	913.1	671.82	885.21	Fracture	845.04	986.19	987.12	903.58	Impermeable fault

Table C-1 (continued)—Geometric coordinates in feet for all fractures and faults in Example 3.

Ali Zidane is a researcher at the Reservoir Engineering Research Institute. His research interests are in the theory and advanced numerical modeling of miscible and immiscible multiphase flows in homogeneous and fractured media and higher-order reservoir simulation of complex subsurface flows. He holds a PhD degree in Earth Sciences from Basel University, Switzerland.

Abbas Firoozabadi is the director of the Reservoir Engineering Research Institute in Palo Alto, California, USA, and a distinguished research professor at Rice University, Houston, Texas, USA. His main research interests are in higher-order reservoir simulations, molecular simulations and molecular engineering in relation to hydrocarbon energy production, and the stewardship of the environment. He holds a BS degree from the Ababan Institute of Technology, Abadan, Iran, and a PhD degree from the Illinois Institute of Technology, Chicago, Illinois, USA.